Fast radiative transfer parameterisation for assessing the surface solar irradiance: The Heliosat-4 method

Zhipeng Qu, Armel Oumbe, Philippe Blanc, Bella Espinar, Gerhard Gesell, Benoît Gschwind, Lars Klüser, Mireille Lefèvre, Laurent Saboret, Marion Schroedter-Homscheidt, et al.

Meteorologische Zeitschrift, Vol. **26**, No. 1, 33–57 (published online October 14, 2016)

Fast radiative transfer parameterisation for assessing the surface solar irradiance: The Heliosat-4 method

Zhipeng Qu[1,4*], Armel Oumbe[1,5], Philippe Blanc[1], Bella Espinar[1], Gerhard Gesell[2], Benoît Gschwind[1], Lars Klüser[2], Mireille Lefèvre[1], Laurent Saboret[3], Marion Schroedter-Homscheidt[2] and Lucien Wald[1]

[1]MINES ParisTech, PSL-Research University, O.I.E. – Centre Observation, Impacts, Energy, Sophia Antipolis, France
[2]Deutsches Zentrum für Luft- und Raumfahrt e.V. (DLR), Oberpfaffenhofen, Germany
[3]Transvalor, Mougins, France
[4]now at: Environment and Climate Change Canada, Toronto, Canada
[5]now at: Total New Energies, R&D Solar, Paris La Défense, France

(Manuscript received February 1, 2016; in revised form April 26, 2016; accepted April 27, 2016)

Abstract

The new Heliosat-4 method estimates the downwelling shortwave irradiance received at ground level in all sky conditions. It provides the global irradiance and its direct and diffuse components on a horizontal plane and the direct irradiance for a plane normal to sun rays. It is a fully physical model using a fast, but still accurate approximation of radiative transfer modelling and is therefore well suited for geostationary satellite retrievals. It can also be used as a fast radiative transfer model in numerical weather prediction models. It is composed of two models based on abaci, also called look-up tables: the already-published McClear model calculating the irradiance under cloud-free conditions and the new McCloud model calculating the extinction of irradiance due to clouds. Both have been realized by using the libRadtran radiative transfer model. The main inputs to Heliosat-4 are aerosol properties, total column water vapour and ozone content as provided by the Copernicus Atmosphere Monitoring Service (CAMS) every 3 h. Cloud properties are derived from images of the Meteosat Second Generation (MSG) satellites in their 15 min temporal resolution using an adapted APOLLO (AVHRR Processing scheme Over cLouds, Land and Ocean) scheme. The 15 min means of irradiance estimated by Heliosat-4 are compared to corresponding measurements made at 13 stations within the Baseline Surface Radiation Network and being located in the field of view of MSG and in various climates. The bias for global irradiance is comprised between 2 and 32 W m^{-2}. The root mean square error (RMSE) ranges between 74 and 94 W m^{-2}. Relative RMSE values range between 15 % and 20 % of the mean observed irradiance for stations in desert and Mediterranean climates, and between 26 % and 43 % for rainy climates with mild winters. Correlation coefficients between 0.91 and 0.97 are found. The bias for the direct irradiance at normal incidence is comprised between −163 and +50 W m^{-2}. The RMSE ranges from 160 W m^{-2} (29 % of the mean observed irradiance) to 288 W m^{-2} (63 %). The correlation coefficient ranges between 0.67 and 0.87.

Keywords: Surface solar irradiance, radiative transfer, satellite observation, cloud properties, aerosols properties, solar resource

1 Introduction

With respect to solar electricity generation the need of temporally and spatially resolved long-term solar radiation databases has been increasing in recent years. The surface solar irradiance (SSI), also known as the downwelling shortwave irradiance at surface, is defined as the power received from the sun on a horizontal unit surface at ground level. Under concern here is the SSI integrated over the whole solar spectrum, i.e. between 0.3 µm and 4 µm, called total or broadband SSI. The global SSI is the sum of the direct SSI from the direction of the sun, also called the beam SSI, and the diffuse SSI from the rest of the sky vault. Knowledge of the global SSI and its components and of their temporal and geographical distribution is of prime importance for numerous applications in solar energy, namely site selection, potential analysis, grid planning, and the engineering design of solar power plants. Other domains where SSI plays a major role are e.g. weather, climate, biomass, or material sciences.

Several early studies have demonstrated the feasibility of extracting the global solar surface irradiance (SSI) from geostationary satellites images like Meteosat (Tarpley, 1979; Möser and Raschke, 1984). Among several other methods, the original Heliosat method was developed by Cano et al. (1986). It became very popular and the versions bearing major improvements were numbered (Heliosat-1, Beyer et al., 1996; Heliosat-2,

*Corresponding author: Zhipeng Qu, Environment and Climate Change Canada, 4905 Dufferin Street, Toronto, Ontario, M3H 5T4, Canada, e-mail: zhipeng.qu@canada.ca

DOI 10.1127/metz/2016/0781

Rigollier et al., 2004; Heliosat-3). The principles of the Heliosat method describe the case when a cloud exhibits a larger reflectance than the ground. Consequently, the appearance of a cloud in the field of view of the satellite sensor should result in an increase of the perceived signal: the cloud appears brighter than the ground. All previous Heliosat versions have in common to be divided into two parts regarding the physical modelling: converting the satellite image into a cloud index and converting the cloud index in irradiance. Therefore, they are called cloud index methods and use several empirical functions. On the other hand, numerical radiative transfer models (RTM) simulate the propagation of radiation through the atmosphere and are used to calculate the SSI for given atmospheric and surface conditions. RTMs are demanding regarding computer time and inappropriate in cases where satellite based operational computations of the SSI are performed such as at the Deutscher Wetterdienst (Mueller et al., 2009), the Royal Netherlands Meteorological Institute (KNMI) (Deneke et al., 2008; Greuell et al., 2013), or the MINES ParisTech (Blanc et al., 2011). Several solutions have been proposed in order to speed up calculations of the SSI. Among them is the use of abaci – also known as look-up tables (LUT) – (see e.g. Deneke et al., 2008; Huang et al., 2011; Mueller et al., 2009; Schulz et al., 2009). This solution is used here.

The present work was part of the MACC (Monitoring Atmospheric Composition and Climate) projects funded by the European Commission. MACC was preparing European Commission's Copernicus Atmosphere Monitoring Service (CAMS) aiming at the operational provision of freely available geo-information from remote sensing and associated geophysical modelling. To that purpose, the new method Heliosat-4 has been developed that benefits on the one hand from the capabilities of the Meteosat satellites to monitor clouds and their optical properties, and on the other hand, from the recent advances on atmosphere composition modelling made in MACC projects. The latter are preparing the operational provision of global aerosol properties analyses and forecasts together with physically consistent total column content in water vapour and ozone (Benedetti et al., 2011; Kaiser et al., 2012; Peuch et al., 2009). Such 3-h resolved information has not been available so far from any operational numerical weather prediction (NWP) centre.

This paper describes the methodology chosen, its practical implementation, its strengths, its current weaknesses and restrictions. It also provides a validation against ground measurements. The concept of Heliosat-4 is discussed in Section 2. Section 3 presents an overview of the clear-sky model estimating the SSI under cloudless skies, hereafter called clear-sky conditions. The model for cloudy sky and its input data are described in Section 4 and its implementation in Section 5. Section 6 describes the ground-based measurements from 13 Baseline Surface Radiation Network (BSRN) stations used for validation as well as the protocol of validation. The results of this station-wise validation are presented in Section 7 followed by detailed discussions of the sources of errors in Heliosat-4 in Section 8 which summarizes the work and discusses the applicability and limits of Heliosat-4 in its current status.

2 The concept of Heliosat-4

Let G denote the global SSI received on a horizontal surface for any sky, i.e. all sky conditions, including both clear (being cloud-free) and cloudy conditions. G is the sum of the direct SSI B and diffuse SSI D. In the present article, B does not comprise the circumsolar radiation. This is contrary to the definition of WMO on direct irradiance being defined as the irradiance measured by a pyrheliometer. These differences are deeply discussed in Blanc et al. (2014a). Let note G_c, B_c and D_c the same quantities but for clear-sky conditions. Let KT, KT_B, KT_c and KT_{Bc} be respectively, the clearness index and the direct clearness index for all-sky conditions and clear-sky conditions:

$$\begin{aligned} KT &= G/E_0 \\ KT_B &= B/E_0 \\ KT_c &= G_c/E_0 \\ KT_{B_c} &= B_c/E_0 \end{aligned} \tag{2.1}$$

where E_0 denotes the irradiance received on a horizontal surface at the top of atmosphere for the location and time under concern. The readers are referred to the appendix for a complete list of symbols.

According to Lefèvre et al. (2013), G_c, B_c and D_c are functions of the solar zenith angle θ_S and of clear atmosphere properties. The latter are denoted P_c and form a set of 7 variables governing the optical state of the atmosphere in clear-sky: *i)* total column contents in ozone and *ii)* water vapour, *iii)* elevation of the ground above mean sea level, *iv)* vertical profile of temperature, pressure, density, and volume mixing ratio for gases as a function of altitude, *v)* aerosol optical depth (AOD) at 550 nm, *vi)* Ångström coefficient, and *vii)* aerosol type. In addition, Lefèvre et al. (2013) note that G_c and D_c are functions of the ground albedo ρ_g.

K_{cG} and K_{cB} denote the clear-sky indices and are defined as the ratio of the actual to the clear sky irradiances:

$$\begin{aligned} G &= G_c(\theta_S, \rho_g, P_c) K_{cG}(\theta_S, \rho_g, P_c, P_{\text{cloud}}) \\ B &= B_c(\theta_S, P_c) K_{cB}(\theta_S, P_c, P_{\text{cloud}}) \end{aligned} \tag{2.2}$$

P_{cloud} is a set of variables describing the properties of the clouds and will be discussed later in Section 4.2. K_{cG} and K_{cB} are also often called cloud modification factor in studies on erythemal UV or photosynthetically active radiation (e.g. Calbo et al., 2005; den Outer et al., 2010).

K_{cG} and K_{cB} describe the cloud influence on the downwelling radiation and are expected to change

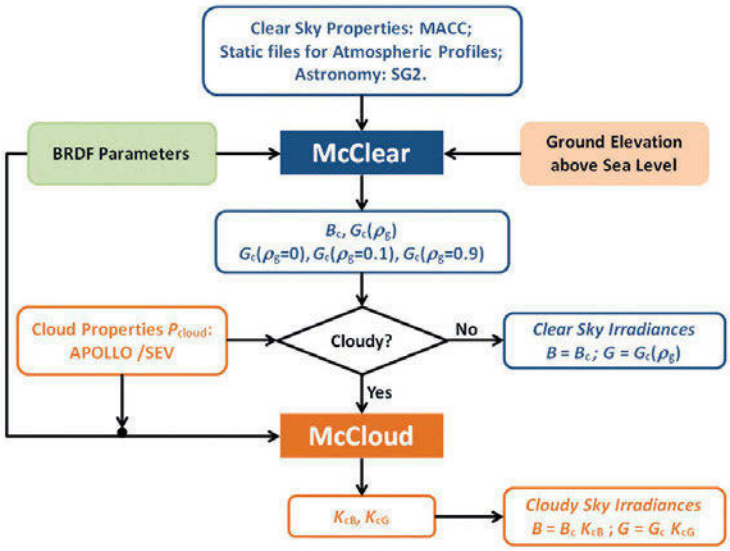

Figure 1: Schematic structure of the Heliosat-4 method.

also with clear atmosphere properties P_c since clouds, aerosols and gases are present in the same atmospheric column and all interact with the radiation field at the same time. Nevertheless, Oumbe et al. (2014) found based on an extensive numerical study with two RTMs that for all considered cloud properties, and a large range of θ_S and ρ_g, the influence of changes in P_c on K_{cG} and K_{cB} is generally less than 2–5 %, provided $\rho_g < 0.7$. In these cases the first derivatives $\partial K_{cG}/\partial P_c$ and $\partial K_{cB}/\partial P_c$ are close to 0. This range is similar to the typical uncertainty associated to the most accurate pyranometers (WMO, 2008). According to Oumbe et al. (2014) the following approximations may be adapted with an error (P95) on G and B less than 15 W m^{-2}:

$$\begin{aligned} G &\approx G_c(\theta_S, \rho_g, P_c) K_{cG}(\theta_S, \rho_g, P_{c0}, P_{\text{cloud}}) \\ B &\approx B_c(\theta_S, P_c) K_{cB}(\theta_s, P_{c0}, P_{\text{cloud}}) \end{aligned} \tag{2.3}$$

where P_{c0} is an arbitrarily chosen set P_c which replaces the variable P_c by a fixed and typical set of clear-sky variables.

In case of long paths of sun rays in the atmosphere, the influence of clear-atmosphere properties on K_{cG} and K_{cB} is not negligible anymore. The relative error made when using (2.3) can reach significant values at large θ_S with 4 % at 70 ° and 8 % at 80 °, especially when $\rho_g > 0.7$. However, in such cases, the irradiances are very low, and the absolute error on G and B expressed as the percentile 95 % (P95) is less than 15 W m^{-2}. The P95 can be greater than 15 W m^{-2} when $\rho_g > 0.7$ (Oumbe et al., 2014). In that case, one should be cautious in using (2.3). Such large albedos are rarely found, but may occur in cases of fresh snow.

Oumbe et al. (2014) have studied the selection of the typical set P_{c0}. They found that the difference in K_{cG} and K_{cB} using different typical sets P_{c0} was negligible, provided that the selected P_{c0} does not include extreme values. They recommended the following set which has been implemented here:

- The mid-latitude summer atmosphere from the USA Air Force Geophysics Laboratory (AFGL) data sets is taken for the vertical profile of temperature, pressure, density, and volume mixing ratio for gases as a function of altitude.
- AOD at 550 nm is set to 0.20, Ångström coefficient is set to 1.3, and aerosol type is continental average.
- Total column water vapour content is set to 35 kg m^{-2}.
- Total column ozone content is set to 300 Dobson units.
- Elevation above sea level is 0 m.

Therefore, computations of the SSI in Heliosat-4 can be made by considering independently the clear-sky conditions and the cloudy conditions as shown in Eq. (2.3). Two independent models were developed and used, one for clear-sky conditions that provides the quantities G_c and B_c, and the other for cloudy conditions that provides the quantities K_{cG} and K_{cB}. Each model has its own set of inputs. This allows efficient usage of cloud and clear-sky variables available at different spatial and temporal resolutions. When both models are abaci-based, using (2.3) means using two ensembles of abaci, one for clear-sky and the other for cloudy skies. In doing so, the number of entries for each ensemble is reduced leading to reducing *i)* the size of the abaci, *ii)* the number of combination between parameters, and *iii)* the total number of interpolations between nodes, thus increasing the speed in computation.

The clear-sky model McClear (Lefèvre et al., 2013) estimates G_c and B_c, and the cloudy sky model McCloud estimates K_{cG} and K_{cB}. Both models are detailed hereafter. Fig. 1 exhibits a schematic structure of Heliosat-4. The clear-sky computations are performed first and then the computations of K_{cG} and K_{cB} if clouds are present.

3 Overview on the McClear model and its inputs

The McClear model has already been published (Lefèvre et al., 2013) and its derivation is not detailed here. It is a physics based model established on the basis of the radiative transfer model libRadtran (Mayer and Kylling, 2005; Mayer et al., 2010). It provides the broadband SSI and its components under clear sky conditions. It accurately reproduces the irradiance computed by libRadtran with a computational speed being approximately 10^5 times faster by using the abaci approach combined with interpolation functions.

An abacus contains results of a libRadtran computation for selected values of the inputs, the so-called node points. Interpolation functions permit to interpolate the libRadtran results stored in the abacus between node points to yield results for any values of the inputs. Actually, the McClear abaci comprise the clearness index KT_c for ρ_g equal to 0, 0.1, and 0.9, and the direct clearness index KT_{Bc} for $\rho_g = 0$. A specific method is used for the interpolation of the ground albedo (Lefèvre et al., 2013). The choice of using only three different values of ρ_g (0, 0.1 and 0.9) reduces the size of LUTS, but also guarantees the best performance for the full albedo range from 0 to 1.

Based on the input data availability in CAMS, McClear delivers time-series of SSI for any place in the world and any instant starting from 2004. Its inputs are:

- θ_S as provided by the fast algorithm for the solar position SG2 (Blanc and Wald, 2012);
- three parameters describing the bidirectional reflectance distribution function (BRDF) in the Moderate-resolution Imaging Spectroradiometer (MODIS) database (Schaaf et al., 2002) from which ρ_g can be computed. The worldwide climatological monthly means of these three parameters as derived by Blanc et al. (2014b) from the MODIS BRDF/Albedo model parameters product MCD43C1 and MCD43C2 data have been used. This dataset has a spatial resolution of 0.05 °;
- the altitude of the ground level, given by the user, or taken from the SRTM data set (Farr et al., 2007) if available or the GTOPO30 data set (Gesch and Larson, 1996);
- the elevation of the CAMS cell above the ground;
- the AOD at 550 nm from CAMS, and the Ångström coefficient computed from the aerosol optical depths at 550 nm and 1240 nm as provided in CAMS;
- the aerosol type (Hess et al., 1998). CAMS delivers also partial optical depths at 550 nm for dust, organic, sea salt, sulphate, and black carbon aerosol species which are input to the algorithm of Lefèvre et al. (2013) converting the total and partial optical depths into aerosol types: urban, continental clean, continental polluted, continental average, maritime clean, maritime polluted, maritime tropical, Antarctic, and desert;
- the total column contents in ozone and water vapour given by CAMS;
- the vertical profiles of temperature, pressure, density, and volume mixing ratio for gases as a function of altitude, which are those from the USA Air Force Geophysics Laboratory (AFGL, Anderson et al., 1986) as implemented in libRadtran: tropics, mid-latitude summer and winter, and sub-Arctic summer and winter. A zoning has been constructed for the automatic selection of the atmospheric profile for any site based on the Koeppen climate classification map (Lefèvre et al., 2013). In order to avoid spatial discontinuity due to the abrupt change in vertical profiles, the original algorithm of Lefèvre et al. (2013) has been improved. McClear computes G_c and B_c for each profile and averages these estimates weighted by the inverse of the distance of the site of interest to the closest border of each zone. The period ranging from November to April is considered as boreal winter and austral summer.

McClear has been previously validated with respect to 1 min measurements of G and B, detected as corresponding to clear sky condition, from the Baseline Surface Radiation Network (BSRN; Ohmura et al., 1998). Measurements used were collected from 11 sites located throughout six continents (Lefèvre et al., 2013). The bias for G_c comprises between −6 and 25 W m^{-2} depending on the station, that is between −1 % to 4 % of the mean of the measurements for the station. The root mean square error (RMSE) ranges from 20 W m^{-2} (3 % of the mean observed irradiance) to 36 W m^{-2} (5 %) and the correlation coefficient ranges between 0.95 and 0.99. The bias for B_c comprises between −48 and +33 W m^{-2}. The RMSE ranges from 33 W m^{-2} (5 %) to 64 W m^{-2} (10 %). The correlation coefficient ranges between 0.84 and 0.98.

Additional validation was performed by Eissa et al. (2015a) with cloud-free measurements made every 10 min at 7 sites in the United Arab Emirates where cloud-free skies are often turbid. The bias for G_c comprises between −9 W m^{-2} (−1 %) and 35 W m^{-2} (6 %). The RMSE ranges from 22 W m^{-2} (4 %) to 47 W m^{-2} (8 %) and the correlation coefficient ranges between 0.990 and 0.995. The bias for B_c comprises between −57 W m^{-2} (−8 %) and 6 W m^{-2} (1 %). The RMSE ranges from 62 W m^{-2} (9 %) to 87 W m^{-2} (13 %). The correlation coefficient ranges between 0.911 and 0.929.

Eissa et al. (2015b) compared McClear estimates with hourly measurements made in 7 sites in Egypt measuring G with two of them measuring B as well. The bias for G_c comprises between 33 W m^{-2} (4 %) and 91 W m^{-2} (12 %). The RMSE ranges from 48 W m^{-2} (6 %) to 105 W m^{-2} (14 %) and the correlation coefficient ranges between 0.941 and 0.982. The biases for B_c are -21 W m^{-2} (−2 %) and 31 W m^{-2} (4 %). The RMSE are 63 W m^{-2} (8 %) and 96 W m^{-2} (13 %). The correlation coefficient is 0.727 for the southernmost station, but is only 0.205 for the Cairo megacity.

4 McCloud: modelling the clear-sky indices

4.1 The influence of cloud properties

As shown in Eq. (2.2) and (2.3), information on cloud properties is needed in order to calculate K_{cG} and K_{cB}. However, not all necessary information on cloud properties is operationally available nowadays from the geostationary satellites at the required temporal and spatial resolution. The design of McCloud aims at a trade-off between the relevance of a cloud property and its operational availability.

Cloud properties such as cloud optical depth τ_{cloud} and cloud phase have strong impacts on K_{cG} and K_{cB} and others have been shown to only weakly impact K_{cG} and K_{cB} (Oumbe, 2009; Qu, 2013). The set of variables describing the properties of the clouds P_{cloud} comprises: *i)* cloud optical depth τ_{cloud}, *ii)* cloud phase, *iii)* liquid/ice water content, *iv)* droplet effective radius, and *v)* the vertical position of the cloud. More precisely, Oumbe (2009) and Qu (2013) have shown by using the RTM libRadtran that changes in cloud liquid/ice water content and droplet effective radius have limited impact on the estimated SSI. In the specific case of CAMS, very limited information on the cloud liquid/ice water content and effective droplet radius is available up to now for the complete database starting in 2004. Considering the unavailability of the data and their limited impact, typical values are selected. They are set to 0.005 g m^{-3} and 20 µm for ice clouds and 1.0 g m^{-3} and 10 µm for water clouds (Oumbe et al., 2014).

Oumbe et al. (2014) established Eq. (2.3) by a methodology based on Monte-Carlo statistical analysis. Seven typical geometric positions of water clouds and three of ice clouds were tested in combination with 20 000 physically-consistent – i.e. with realistic probability distribution functions – compositions of θ_S, ρ_g, τ_{cloud} and P_c, yielding 140 000 values for G, B, K_{cG} and K_{cB} for water clouds and 60 000 for ice clouds. The same data were used here to study the influence of the heights of the cloud base and cloud top on the SSI estimated by the RTM libRadtran. As is done in the majority of satellite retrievals, only single layer clouds were assumed in this analysis.

The first result of the statistical analysis is that unsurprisingly, in cloudy skies, τ_{cloud} is the variable within P_{cloud} having the greatest impact on G, D and B. Fig. 3 exhibits an example of variation of B and D with τ_{cloud}, for water and ice clouds and for the seven cases for water clouds and the three for ice clouds. Other inputs to libRadtran have been kept constant. One observes a strong dependency of B and D with τ_{cloud}. B decreases sharply with τ_{cloud} and reaches 0 for τ_{cloud} around 5 (Fig. 2a). Expectedly for a given τ_{cloud}, B does not change with the cloud phase, ground albedo or height of the cloud base or top. This is confirmed when using different clear-atmosphere properties P_c and θ_S as inputs.

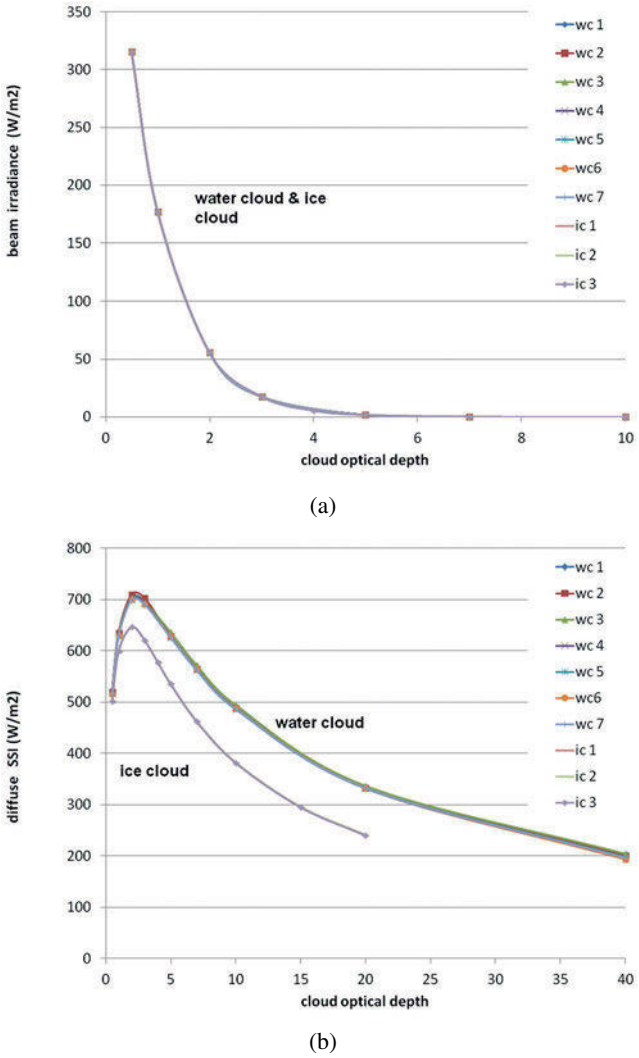

Figure 2: Changes in B (a) and D (b) with τ_{cloud}, for water and ice cloud types, various heights of the cloud base and top. θ_S is 30 °, aerosol optical depth at 550 nm is 0.5, and ρ_g is 0.2. *wc* means water clouds, and *ic* ice clouds. Numbers, e.g. *wc1*, refer to the seven water cloud and the three ice cloud cases.

One observes in Fig. 2b that D rises sharply as τ_{cloud} increases from 0 up to 2–3 and then decreases as τ_{cloud} increases for both water and ice clouds. The global G decreases slowly as τ_{cloud} increases from 0 up to 2–3 and this increase in D compensates the strong decrease in B. The different ice clouds cases (ic1, ic2, ic3) cannot be distinguished. This is also true for water clouds but to a lesser extent. The influence of the cloud geometrical properties on D is very small. Further analysis showed that the variance $v(D)$ computed on the series of D obtained for each of the 20 000 combinations (θ_S, ρ_g, τ_{cloud}, P_c) is small with respect to the squared mean of D when $\rho_g < 0.5$, meaning that changes in D with varying cloud vertical position and extension are small. The root of the mean of $v(D)$ is less than 5 W m^{-2} for water cloud and 2 W m^{-2} for ice cloud. Only the extreme cases with the combination of large albedo ($\rho_g > 0.9$) and large cloud optical depth ($\tau_{\text{cloud}} > 40$) cause relatively greater

root of the mean of $v(D)$: 20 W m^{-2} for water cloud and 7 W m^{-2} for ice cloud.

The larger variation for the extreme cases may be explained by the enforcement of the multiple reflections of radiation between the surface and the cloud occurring when ρ_g and τ_{cloud} are both large. In this case, more interactions occur between the radiation and aerosols, water vapour, and other gases. The change of the cloud geometric position, i.e. cloud base height, has a stronger impact on D in such cases. However, these extreme cases are rare, e.g. they are less than 1 % for all measurements being used for validation later on. Therefore, it can be considered that for the majority of cases, the influence of the cloud vertical position and extent is small or negligible.

Even if the influence of vertical position of cloud is small or negligible for the radiative transfer, it is nevertheless preferable to avoid systematic – even small – errors due to systematic error in the vertical position and extent of the clouds. Considering the unavailability of descriptors in an operational way, we have used typical vertical positions and extensions depending on the cloud types in the APOLLO/SEV data set discussed later (Section 4.2) that are made operationally available within CAMS.

Four reference categories were thus selected with predefined base heights and geometrical thicknesses:

- low level cloud: water cloud at low altitude, with a base height of 1.5 km and a thickness of 1 km;
- medium level cloud: water cloud at medium altitude, with a base height of 4 km and a thickness of 2 km;
- high level cloud: deep cloud of large vertical extent from low altitude to medium altitude, with a base height of 2 km and a thickness of 6 km;
- thin ice cloud: ice cloud with a base height of 9 km and a thickness of 0.5 km.

Deep clouds, such as *cumulonimbus* which extend vertically from 1 and 2 km up to the tropopause (8–10 km), are mostly composed of water droplets and typically have ice crystals at the cloud top. Currently, they are treated like water clouds based on the expectation that they are optical thick anyhow independent of the cloud phase at the top of the cloud.

For all 140 000 cases for water and 60 000 cases for ice clouds, D^* was computed with the above-mentioned corresponding reference categories and was compared to the actual D computed with the exact values of vertical positions and extensions. For each triplet $(\theta_S, \rho_g, \tau_{\text{cloud}})$ the differences $(D^* - D)$ were summarized by the bias and the root mean square difference (RMSD) for water clouds on the one hand, and ice clouds on the other hand. The mean, P5 and P95 of the biases and RMSD were computed for each θ_S and are shown in Fig. 3.

A decrease of RMSD and bias with θ_S is observed. For water clouds, the mean of RMSD and bias range from 5 W m^{-2} for $\theta_S = 0\,^\circ$ to 1 W m^{-2} for $\theta_S = 80\,^\circ$ and from 5 W m^{-2} to −1 W m^{-2}, respectively. The P95 of RMSD and bias are always less than 14 W m^{-2} and decrease towards 0 W m^{-2} as θ_S increases. Lower deviations are obtained under ice clouds. Means of RMSD and bias range from 2 W m^{-2} for $\theta_S = 0\,^\circ$ to 0 W m^{-2} for $\theta_S = 80\,^\circ$. The P95 of RMSD and bias are less than 9 W m^{-2} and decrease towards 0 W m^{-2} as θ_S increases.

In both cases, the relative P95 is always less than 1 %. It can be concluded that the combination of the cloud base height, the cloud geometrical thickness and the cloud phase can be aggregated into four reference categories with a negligible error on the modelled D. This is of practical interest since the geometry and heights of the clouds are typically unknown.

This conclusion is limited to the ideal cases in libRadtran where clouds are infinite and made of plane-parallel layers. The representation of ice cloud optical properties follows Fu (1996) and Fu et al. (1998) as implemented in libRadtran. In reality three-dimensional cloud effects as e.g. the parallax effect (Schutgens and Roebeling, 2009; Greuell and Roebeling, 2009) and the overshooting (Schade et al., 2007) of global irradiances are observed. These effects are also very sensitive to the geometrical height, the extension and the overall structure of the cloud, but cannot be treated by plane-parallel radiative transfer simulations. Nevertheless, in the operational geostationary satellite-based irradiance retrievals, the necessary input on three-dimensional cloud structures is mostly unavailable. Therefore, these effects are not included here.

4.2 Cloud properties used in McCloud: APOLLO/SEV

The APOLLO (AVHRR Processing scheme Over cLouds, Land and Ocean; Kriebel et al., 1989; Kriebel et al., 2003) algorithm was originally developed to exploit data from the AVHRR sensors aboard the polar orbiting series of NOAA satellites, in order to estimate the properties of clouds. It has been adapted to process images of the SEVIRI (Spinning Enhanced Visible and Infrared Imager) instrument aboard the series of MSG satellites. This adaptation is named APOLLO/SEV. The APOLLO scheme has to be adapted for each sensor it is applied to. Moreover the thresholds for cloud detection vary with the geographical region. Compared to the APOLLO for NOAA-AVHRR, the following changes were made: defaults of thresholds for most of the APOLLO/SEV tests have been re-defined depending on the region being visible by SEVIRI and especially for non-European areas. Additionally, APOLLO/SEV contains an updated correction database for masking regional peculiarities as e.g. cold currents and thermal fronts in the ocean, deserts with airborne dust, or known bright surfaces as dry lakes, etc. Since the received radiation in the 0.6 µm channel of SEVIRI is subject to only a small amount of water vapour absorption, it can be similarly used for derivation of τ_{cloud} as in previous APOLLO schemes. A check if results of APOLLO/SEV are reasonable has been done

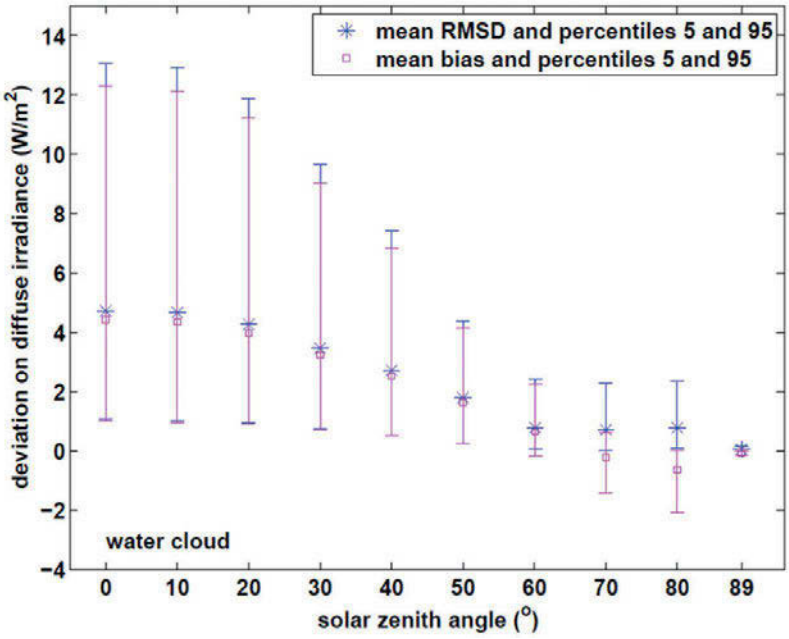

(a)

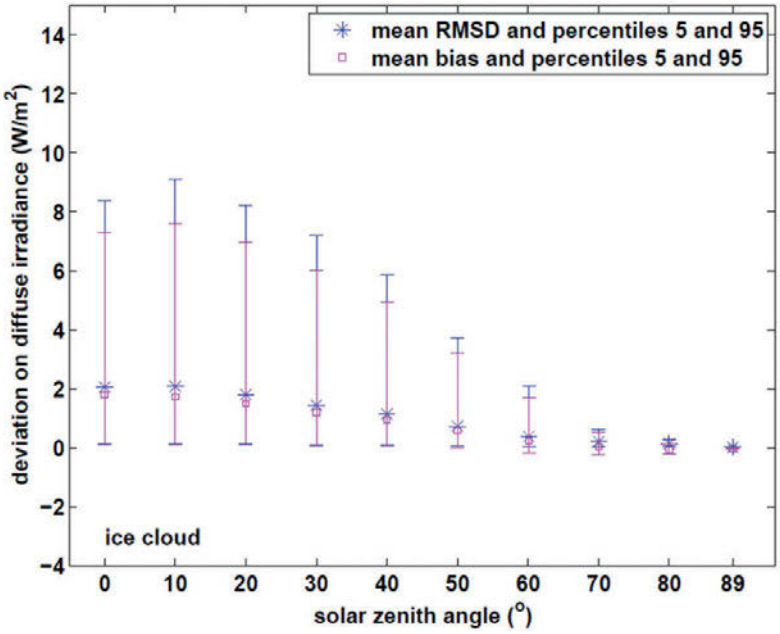

(b)

Figure 3: Error made when computing D using reference categories of clouds as (a) water clouds and (b) ice clouds.

by means of comparisons of cloud properties derived from both, SEVIRI and AVHRR, in coincident scenes (WDC, 2015). APOLLO/SEV provides quantities related to clouds for each pixel (3 km at nadir) and every 15 min. Among these quantities, a mask with values being cloud-free or cloudy, τ_{cloud} and the level of the cloud as being low, medium, or high, together with additionally a thin cloud type class, are derived. Cloud types are defined according to the cloud top temperature. The layer boundaries are set to 700 hPa and 400 hPa with the associated temperatures taken from standard atmospheres. The thin clouds layer exclusively contains thin pure ice phase clouds with no thick clouds underneath. Fully and partly cloudy pixels are discriminated. Cloud coverage, i.e. the fraction of a pixel covered by a cloud, expressed in percent, is derived for each level and the thin class of clouds separately. The cloud coverage is calculated at daytime by the relationship between the reflectance measured at 0.6 µm and 0.8 µm and the average reflectances for fully covered and cloud-free pixels in a region of 58 × 58 pixels centred on the pixel under concern. Inside APOLLO/SEV, any τ_{cloud} being less than 0.5 for a fully cloud covered pixel is clipped to 0.5 assuming this as the minimum sensitivity of the optical

depth retrieval for a cloud in order to discriminate from aerosols.

Since APOLLO provides τ_{cloud} only for fully cloudy pixels, a post-processor is applied to estimate τ_{cloud} for partly cloudy pixels. The estimated optical depth of the partly covered pixel is computed firstly by taking the average of all τ_{cloud} of the fully covered pixels of same type of cloud in this region, and then by multiplying this average by the cloud coverage. Following the previously chosen definition of a minimum optical depth for any cloud-affected pixel, τ_{cloud} in partly covered pixels is also clipped to a minimum value of 0.45. The value of 0.45 has been chosen being close to the 0.5 value discussed above but also being able to identify those cases afterwards from the value itself. Otherwise, the pixel is considered as cloud-free. The impact of this decision is further discussed in Section 8.5. The maximum τ_{cloud} is set at 500.

4.3 The concept of McCloud

The inputs to McCloud are:

- θ_S that is computed as for McClear;
- the three parameters describing the BRDF from which ρ_g can be computed as detailed hereafter. Similarly to McClear, the worldwide climatological monthly means of these three parameters proposed by Blanc et al. (2014b) has been used;
- τ_{cloud} from APOLLO/SEV for the pixel under concern;
- cloud type from APOLLO/SEV from which the clouds are allotted to one of the four reference categories: low, medium, high, and thin ice cloud.
- cloud coverage (mask) from APOLLO/SEV.

McCloud is composed of two modules. The first one is an analytical module and is designed to compute K_{cB} which is a function of the cloud optical depth τ_{cloud} and θ_S as illustrated in Fig. 2a:

$$K_{cB} = \exp[-\tau_{\text{cloud}}/\cos(\theta_S)] \tag{4.1}$$

The second module is an abaci-based module designed to compute K_{cG}. The abaci have a limited number of inputs because they are computed with a single typical P_{c0} as presented previously (Section 2), and have consequently a small size which helps to reduce computational effort.

4.4 The abaci for global irradiance

Four abaci were constructed containing values of K_{cG}, one for each cloud reference category. These abaci were computed by running libRadtran with the solver 'disort 16-stream' and the representation of ice cloud optical properties (Mayer et al., 2010). K_{cG} is computed for each node from two runs of libRadtran, one for clear-sky, one for cloudy sky:

$$K_{cG}(\theta_S, \rho_g, P_{c0}, P_{\text{cloud}}) = G(\theta_S, \rho_g, P_{c0}, P_{\text{cloud}})/G_c(\theta_S, \rho_g, P_{c0}) \tag{4.2}$$

The choices of node points for each of the three variables (θ_S, τ_{cloud}, ρ_g) in the abacus were firstly examined. A bi-linear interpolation of K_{cG} with respect to θ_S and τ_{cloud}, and a specific interpolation with respect to ρ_g (Subsection 5.1) were performed for a large number of possible random compositions of the other atmospheric properties. The interpolation results were compared to the results of libRadtran serving as reference. The choice was based on an empirically-defined trade-off between a limited number of node points and an accurate assessment by the interpolation functions (Qu, 2013).

The selected node points are:

- θ_S (deg): 0, 5, 10, 15, 20, 25, 30, 35, 40, 45, 50, 55, 60, 65, 70, 75, 80, 85, 89
- τ_{cloud}: 0.1, 0.5, 1, 2, 3, 4, 6, 8, 10, 13, 16, 20, 25, 30, 37, 45, 55, 65, 75, 90, 110, 140, 180, 230, 290, 370, 500
- ρ_g: 0, 0.1, 0.9 (as further discussed in Section 5.1)

For completeness reasons, node points include large values of θ_S above 75 ° and for τ_{cloud} above 100 even if their practical relevance in our application is restricted due to highly inaccurate satellite retrievals under these conditions.

For θ_S, τ_{cloud}, ρ_g considered separately, the interpolation results exhibit a bias less than 0.4, 1.5, 0.2 W m^{-2} and a RMSE less than 0.4, 1.5, 0.4 W m^{-2}. Eventually, the performance of the interpolation was assessed with all the three variables together for different possible compositions of clear-sky properties; the bias is about 0.5 W m^{-2} and the RMSE around 1 W m^{-2} (Qu, 2013). These values are small and similar to the sensitivity of measuring instruments of the highest quality classes (WMO, 2008). This choice for the node points and the related interpolation is therefore justified.

If the input is outside the above-mentioned range, an extrapolation is performed. Linear interpolations are performed for θ_S and τ_{cloud}. The order in the sequence of interpolations has a negligible influence on the results. For the sake of computing speed, linear interpolations are performed first, followed by the computation of the ground albedo. Similarly to the McClear abaci, the McCloud abaci comprise the clear-sky indices K_{cG} for ρ_g equal to 0, 0.1, and 0.9, and the direct clearness index K_{cB} for a zero albedo.

5 Practical implementation of Heliosat-4

5.1 Interpolation within the McCloud abacus

The two first interpolations on θ_S and τ_{cloud} provide three values of K_{cG}, one for each ρ_g = 0, 0.1, and 0.9. McClear provides the corresponding three values of G_c. G is computed for each of the three ρ_g as follows:

$$G(\theta_S, \rho_g, P_{c0}, P_{\text{cloud}}) = G_c(\theta_S, \rho_g, P_{c0}) K_{cG}(\theta_S, \rho_g, P_{c0}, P_{\text{cloud}}) \tag{5.1}$$

The formula of Vermote et al. (1997) applies to the clearness index KT:

$$KT(\rho_g) = KT(\rho_g = 0)/(1 - \rho_g S_{\text{cloud}}) \tag{5.2}$$

It describes the change in KT as a function of the ground albedo ρ_g and the spherical albedo S_{cloud} of the cloudy atmosphere. At this step, ρ_g has three values: 0, 0.1, and 0.9 while S_{cloud} is unknown. In principle, S_{cloud} can be computed knowing KT for any value of ρ_g using Eq. (5.2). In practice, better results are attained if S_{cloud} is computed for two values of ρ_g: 0.1 and 0.9 using Eq. (5.2):

$$\begin{aligned} S_{\text{cloud}}(\rho_g = 0.1) &= [1 - G(\rho_g = 0)/G(\rho_g = 0.1)]/0.1 \\ S_{\text{cloud}}(\rho_g = 0.9) &= [1 - G(\rho_g = 0)/G(\rho_g = 0.9)]/0.9 \end{aligned} \tag{5.3}$$

from which one obtains:

$$\begin{aligned} a &= [S_{\text{cloud}}(\rho_g = 0.9) - S_{\text{cloud}}(\rho_g = 0.1)]/0.8 \\ b &= S_{\text{cloud}}(\rho_g = 0.1) - 0.1a \end{aligned} \tag{5.4}$$

and eventually

$$S_{\text{cloud}} = a\rho_g + b \tag{5.5}$$

Eq. (5.1) may be rewritten:

$$G(\theta_S, \rho_g, P_c, P_{\text{cloud}}) = \frac{G(\rho_g = 0)}{1 - \rho_g S_{\text{cloud}}} = \frac{G_c(\theta_S, \rho_g = 0, P_c) K_{cG}(\theta_S, \rho_g = 0, P_{c0}, P_{\text{cloud}})}{1 - \rho_g S_{\text{cloud}}} \tag{5.6}$$

where the only remaining unknown is ρ_g.

The choice of the ground albedo values of 0.1 and 0.9 is that of the McClear model (Lefèvre et al., 2013). With these two values, G and the spherical albedo S_{cloud} of the cloudy atmosphere can be calculated accurately for any ground albedo from 0 to 1. This combination of Eq. (5.3)– (5.6) largely outperforms any linear interpolation made with more fitting points.

The ground albedo ρ_g is computed in the same way as in Lefèvre et al. (2013). Blanc et al. (2014b) created a worldwide climatological complete database containing monthly means of the three BRDF parameters, called $f$iso, $f$vol, and $f$geo (Schaaf et al., 2002). This database is available at http://www.oie.mines-paristech.fr/Valorisation/Outils/AlbedoSol/. In any operational use of the Heliosat-4 approach one may want to use the most recent BRDF maps in order to take year-to-year variations of the most recent data period into account. Lefevre et al. (2013) discussed the two approaches (near-real-time and climatology) in the case of McClear. They reported that when compared to ground-based measurements of the SSI, both approaches gave the same results with very small differences not taking into account the gaps. They have adopted the climatology approach because it makes easier the implementation of McClear. The same is done here.

$f$iso describes the isotropic part of the BRDF; the two other parameters are linked to the viewing and illuminating geometry to describe the anisotropic part of the BRDF. The directional hemispherical reflectance ρ_{bs} and the bihemispherical reflectance ρ_{ws} are computed from the BRDF using formulas in Schaaf et al. (2002). The parameters ρ_{bs} and ρ_{ws} are also known as black sky and white sky albedo (e.g. Schaepman-Strub et al., 2006). The ground albedo ρ_g is given by:

$$\rho_g = \rho_{ws} D/G + \rho_{bs} B/G \tag{5.7}$$

In the presence of cloud, ρ_g is not the same as that calculated by McClear and must be computed again. The major difficulty in Eq. (5.7) is that ρ_g depends upon $D(\rho_g)$ and $G(\rho_g)$ which depend themselves on ρ_g. At this step, B, and accordingly KT_B, are known, and the method proposed by Lefèvre et al. (2013, Eq. 8) can be used to solve the problem. Eq. (5.7) may be rewritten as:

$$\rho_g = \rho_{ws} + (\rho_{bs} - \rho_{ws})(KT_B/KT(\rho_g)) \tag{5.8}$$

By using KT instead of G, then combining Eqs. (5.4)–(5.6) and Eq. (5.8), and denoting $\Delta = (\rho_{bs} - \rho_{ws})$, one obtains a second-order equation in KT which is the quantity of interest:

$$\begin{aligned} &a\Delta^2 KT_B^2 + \\ &\quad KT[KT(\rho_g = 0) + (2a\rho_{ws} + b)\Delta KT_B] + \\ &\quad (a\rho_{ws}^2 + b\rho_{ws} - 1)KT^2 = 0 \end{aligned} \tag{5.9}$$

Using the Monte-Carlo technique to select randomly 100 000 samples, it was found that Eq. (5.8) has only one solution that respects $KT > KT_B$, i.e. $G > B$. Therefore, Eq. (5.9) is used to compute KT and Eq. (5.8) provides the actual ρ_g. In a practical manner, once a request is made for a given site, the three BRDF parameters $f$iso, $f$vol, and $f$geo are taken from the closest grid point in the data set of Blanc et al. (2014b). There is one value of each parameter per month which is allotted to the middle of the day of the middle of the month. A linear interpolation yields $f$iso, $f$vol, and $f$geo for each minute of the day. Then, Eq. (5.9) is solved for KT for each minute.

5.2 Computing SSI for any site

Aerosol properties, and total column contents of water vapour and ozone in CAMS are given every 3 h, starting at 00:00 UTC. The ordering of interpolation of parameters was found as having a negligible influence on the results (Lefèvre et al., 2013). A bi-linear spatial interpolation in space is applied to compute a time-series of 3 h values for the given location. A further linear interpolation in time is performed yielding time-series of these atmospheric quantities every 1 min. These 1 min values are inputs to the McClear model. The 1 min temporal resolution has been chosen as it reflects the variability of irradiation due to the solar position sufficiently well. In addition, it permits to answer needs of users of such

Table 1: List of BSRN stations used for the validation ordered by decreasing latitude

Station	Code	Country	Latitude	Longitude	Elevation a.s.l. (m)	Period
Lerwick	LER	UK	60.133	−1.183	84	2004–2007
Toravere	TOR	Estonia	58.254	26.462	70	2004–2014
Lindenberg	LIN	Germany	52.210	14.122	125	2004–2007
Cabauw	CAB	Netherlands	51.971	4.927	0	2005–2014
Camborne	CAM	UK	50.217	−5.317	88	2004–2007
Palaiseau	PAL	France	48.713	2.208	156	2005–2013
Payerne	PAY	Switzerland	46.815	6.944	491	2004–2011
Carpentras	CAR	France	44.083	5.059	100	2004–2014
Cener	CEN	Spain	42.816	−1.601	471	2009–2013
Sede Boqer	SBO	Israel	30.905	34.782	500	2004–2012
Izana	IZA	Spain	28.309	−16.499	2373	2009–2014
Tamanrasset	TAM	Algeria	22.780	5.51	1385	2004–2014
De Aar	DAA	South Africa	−30.667	23.993	1287	2004

SSI data, especially in the solar energy domain. The abacus for the given atmospheric profile and aerosol type is applied. A series of interpolations is performed to yield KT_{Bc} and KT_c for three ρ_g (= 0, 0.1, 0.9). θ_S and E_0 are computed with the SG2 algorithm (Blanc and Wald, 2012) for the middle of the minute. KT_{Bc} and KT_c are computed every 1 min of the day.

Cloud type and τ_{cloud} from APOLLO/SEV are given every 15 min for each pixel of the MSG image. The abacus for the cloud reference category is applied. A series of abacus-internal interpolations is performed to yield K_{cB} and K_{cG} for three ρ_g (= 0, 0.1, 0.9) for the 1 min that contains the exact instant of the view of the specific pixel. K_{cB} is computed, and then KT_B knowing that $KT_B = K_{cB}\ KT_{Bc}$. KT_{Bc} is taken for the corresponding minute. KT_B, $K_{cG}(\rho_g = 0)$, $K_{cG}(\rho_g = 0.1)$ and $K_{cG}(\rho_g = 0.9)$ are inputs to Eqs. (5.3)– (5.4), (5.8)– (5.9), yielding KT for this minute. Then KT_B and KT are computed every 1 min by linear interpolation. Then, the corresponding SSIB and G are computed every 1 min. In case of no clouds, B and G are respectively equal to B_c and G_c.

6 Data sets for validation

Data sets for validation were collected for 13 stations of the Baseline Surface Radiation Network (BSRN) representing a variety of climates in the field of view of MSG (BSRN snapshot 2014-06 DOI:10.1594/PANGAEA.833428). Table 1 lists these stations, ordered by decreasing latitude. Lerwick, Toravere, Lindenberg, Cabauw, Camborne, Palaiseau, Payerne, and to a lesser extent Cener, experience marine climate with mild winters, constantly moist, noted Cbf in the classification of Trewartha (1954). Carpentras belongs to the Provence region in France, where the sky is often clear and clean. It experiences a climate with mild winters with limited but intense episodes of rain and dry summer (Csa, Mediterranean). Izana and De Aar are located both in high altitude and experience semi-arid climate (BSk). Sede Boqer represents the desert climate (Bwh) while Tamanrasset represents the desert climate (BWh) as well as a mountain climate.

The BSRN is a collection of measurements of G, D, and B_N of high quality suitable for validation. B_N is the direct normal irradiance, being the direct irradiance on a surface always normal to the sun rays ($B = B_N \cos\theta_S$). Measurements were acquired every 1 min for the selected stations and periods. Uncertainty requirements for BSRN data are 5 W m^{-2} for G and 2 W m^{-2} for B_N (Ohmura et al., 1998). Only measurements that are significantly greater than these requirements were used for this validation of Heliosat-4: Values of G less than 10 W m^{-2} and values of B_N less than 4 W m^{-2} were rejected. Quality control procedures described in Roesch et al. (2011) were applied and suspicious measurements removed. In the present study only measurements with θ_S less than 89 ° were used. It is well known that such large θ_S bear large errors in any satellite-based irradiance retrieval. Therefore one might argue to exclude these large θ_S for any validation. However in solar energy, the energy production of photovoltaic systems starts already at low sun elevation and omitting those values may result in deviations e.g. in daily sums. Therefore, large θ_S were included as well.

The 1 min measurements were averaged to 15 min means of SSI. Averaging was done only if at least 13 measurements out of the 15 possible values are valid. These 15 min means of SSI were compared to the Heliosat-4 means calculated for the same minutes. Deviations were computed by subtracting the measurements from the corresponding Heliosat-4 estimate. They were summarized by the bias, the standard deviation, the RMSE, and the Pearson correlation coefficient. Relative values are expressed with respect to the mean of the used measurements.

This operation has been performed for G, D, B_N, KT, KT_D and KT_{BN} the clearness indices for the diffuse and direct normal respectively, site per site, with all data pairs merged, and for different classes of G, D, B_N, KT, KT_d and KT_{BN}, θ_S, cloud properties, ρ_g, year and month. Changes in E_0 due to changes in geometry,

Table 2: Comparison between 15 min means of G measured and estimated by Heliosat-4.

Station	Number of samples	Mean observed value W/m^2	Bias W/m^2 (%)	RMSE W/m^2 (%)	Correlation coefficient
Lerwick	47026	195	12 (6 %)	83 (43 %)	0.906
Toravere	148547	219	13 (6 %)	84 (38 %)	0.926
Lindenberg	50197	264	15 (6 %)	89 (34 %)	0.930
Cabauw	148917	258	32 (12 %)	94 (36 %)	0.930
Camborne	52020	271	29 (11 %)	91 (34 %)	0.937
Palaiseau	119326	281	25 (9 %)	88 (31 %)	0.940
Payerne	93730	322	29 (9 %)	88 (27 %)	0.953
Carpentras	160924	379	22 (6 %)	74 (20 %)	0.967
Cener	57590	353	18 (5 %)	92 (26 %)	0.946
Sede Boqer	123200	528	2 (0 %)	78 (15 %)	0.967
Izana	81706	580	11 (2 %)	94 (16 %)	0.960
Tamanrasset	158412	531	12 (2 %)	91 (17 %)	0.961
De Aar	10711	493	8 (2 %)	90 (18 %)	0.963

Table 3: Comparison between 15 min means of Kt measured and estimated by Heliosat-4.

Station	Number of samples	Mean observed value	Bias (%)	RMSE (%)	Correlation coefficient
Lerwick	47026	0.35	0.011 (3 %)	0.150 (43 %)	0.737
Toravere	148547	0.40	0.010 (3 %)	0.148 (37 %)	0.783
Lindenberg	50197	0.42	0.011 (3 %)	0.137 (32 %)	0.803
Cabauw	148917	0.41	0.040 (10 %)	0.139 (34 %)	0.811
Camborne	52020	0.41	0.037 (9 %)	0.134 (33 %)	0.836
Palaiseau	119326	0.42	0.032 (7 %)	0.132 (31 %)	0.829
Payerne	93730	0.47	0.045 (10 %)	0.137 (29 %)	0.837
Carpentras	160924	0.54	0.030 (6 %)	0.114 (21 %)	0.867
Cener	57590	0.50	0.020 (4 %)	0.134 (27 %)	0.826
Sede Boqer	123200	0.62	0.001 (0 %)	0.111 (18 %)	0.819
Izana	81706	0.73	0.006 (1 %)	0.127 (18 %)	0.696
Tamanrasset	158412	0.64	0.021 (3 %)	0.119 (19 %)	0.822
De Aar	10711	0.63	0.007 (1 %)	0.111 (18 %)	0.863

namely the daily course of the sun and seasonal effects, are usually well reproduced by models and lead to a *de facto* correlation between observations and estimates of SSI hiding potential weaknesses. Clearness indices KT, KT_d and KT_{BN} are stricter indicators of the performances of a model regarding its ability to estimate the optical state of the atmosphere. Though KT, KT_d and KT_{BN} are not completely independent of θ_S as they decrease as θ_S increases, the dependency is much less pronounced than in SSI.

A subset, called clear-sky BSRN, was created to better analyse cloud-free conditions. It was made of BSRN data being identified as clear-sky instants following the criteria of Lefèvre et al. (2013).

Heliosat-4 in principle is suited to provide spectrally resolved irradiances, as it is based on a physical radiative transfer treatment. Nevertheless, for the current implementation of Heliosat-4 only abaci for total irradiances exist, i.e. for the spectral range [240, 4606] nm. The spectral range of instruments used in the BSRN network is slightly different: [285, 2800] nm for pyranometers of Kipp & Zonen and [295, 2800] nm for those of Eppley. According to simulations performed with libRadtran, this difference in spectral range induces a bias of 3–8 W m^{-2} in G, i.e. an overestimation by Heliosat-4, which was not corrected for here.

7 Results of the validation

Tables 2–7 report statistical quantities on the deviations between estimates and measurements in G, KT, D, KT_D, B_N and KT_{BN}, for the 13 stations. The correlation coefficient for G (Table 2) is greater than 0.91 in all cases. Expectedly due to the daily cycle being eliminated, the Pearson product-moment correlation coefficient for KT (Table 3) is slightly less but still close to or greater than 0.80, except in Lerwick (0.74) and Izana (0.70). The correlation coefficient for D (Table 4) is close to or greater than 0.80, except for Sede Boqer (0.74), Izana (0.68) and Tamanrasset (0.75). The correlation coefficient for KT_D (Table 5) exhibits more variability, ranging from 0.35 in Toravere to 0.711 in Carpentras. For B_N (Table 6) and KT_{BN} (Table 7), the correlation coefficient is greater than 0.80 and 0.60 respectively, with the exception of Lerwick (0.67 and 0.33), Toravere (0.72 and 0.37), Izana for B_N (0.71) and for KT_{BN}, Sede Boqer (0.47) and De Aar (0.48). It can be concluded that as a whole Heliosat-4 is able to reproduce the changes in global and direct SSI at a 15 min step. At least 82 % of the variance contained in G is well-explained by Heliosat-4. The explained part of variance is 64 % for D and B_N, except extreme cases such as Sede Boqer, Izana and Tamanrasset. The explained part of variance in KT, KT_D and KT_{BN} is less:

Table 4: Comparison between 15 min means of D measured and estimated by Heliosat-4.

Station	Number of samples	Mean observed value W/m^2	Bias W/m^2 (%)	RMSE W/m^2 (%)	Correlation coefficient
Lerwick	46632	131	32 (24 %)	75 (57 %)	0.843
Toravere	147909	99	46 (47 %)	89 (89 %)	0.780
Lindenberg	50199	134	34 (25 %)	81 (61 %)	0.853
Cabauw	148365	144	35 (24 %)	80 (56 %)	0.850
Camborne	51181	151	32 (21 %)	81 (54 %)	0.841
Palaiseau	117870	146	37 (25 %)	80 (55 %)	0.867
Payerne	97667	138	33 (24 %)	78 (57 %)	0.852
Carpentras	160517	123	31 (26 %)	72 (58 %)	0.859
Cener	57202	142	36 (25 %)	82 (58 %)	0.845
Sede Boqer	122640	138	49 (35 %)	92 (67 %)	0.736
Izana	81606	111	−6 (−6 %)	92 (83 %)	0.682
Tamanrasset	158370	172	−14 (−8 %)	92 (53 %)	0.751
De Aar	10676	96	19 (20 %)	71 (74 %)	0.773

Table 5: Comparison between 15 min means of Kt_d measured and estimated by Heliosat-4.

Station	Number of samples	Mean observed value	Bias (%)	RMSE (%)	Correlation coefficient
Lerwick	46632	0.25	0.052 (21 %)	0.134 (54 %)	0.480
Toravere	147909	0.21	0.078 (37 %)	0.154 (73 %)	0.345
Lindenberg	50199	0.24	0.045 (19 %)	0.124 (53 %)	0.522
Cabauw	148365	0.25	0.052 (21 %)	0.122 (50 %)	0.558
Camborne	51181	0.24	0.047 (19 %)	0.117 (48 %)	0.607
Palaiseau	117870	0.24	0.054 (23 %)	0.117 (50 %)	0.609
Payerne	97667	0.23	0.054 (24 %)	0.124 (55 %)	0.595
Carpentras	160517	0.20	0.047 (24 %)	0.103 (52 %)	0.711
Cener	57202	0.22	0.051 (23 %)	0.117 (53 %)	0.644
Sede Boqer	122640	0.19	0.060 (32 %)	0.121 (65 %)	0.532
Izana	81606	0.16	−0.005 (−3 %)	0.117 (72 %)	0.631
Tamanrasset	158370	0.23	−0.009 (−4 %)	0.107 (47 %)	0.585
De Aar	10676	0.14	0.034 (24 %)	0.106 (73 %)	0.626

approximately 64 %, 36 % and 36 %. It shows that more detailed and precise estimates of the clear atmosphere and clouds are still needed for the purpose of a further improved retrieval scheme.

The correlation coefficient for G exhibits a tendency to decrease as θ_S increases but is often greater than 0.8 even for $\theta_S = 80\,°$. Heliosat-4 is less accurate in reproducing changes of SSI for large θ_S. A reason is probably the restricted validity of the plane-parallel approximation made in any radiative transfer simulation code without any explicit treatment of three-dimensional effects for large θ_S. However, the validation of McClear has shown a limited influence of θ_S (Lefèvre et al., 2013). The main cause is more likely a lower accuracy in the retrieval of the cloud properties by satellites for large sun and satellite viewing zenith angles. The northernmost stations (Lerwick, Toravere) exhibit low correlation coefficients. This can be explained by a sun zenith angle being typically greater at solar noon times than in more southern stations and by the large viewing angles of these sites by the SEVIRI sensor, and the more frequent occurrence of clouds.

The bias in G (Table 2) is positive for all stations. It ranges between 8 W m^{-2} (i.e. 2 % of the mean of the measurements) to 29 W m^{-2} (10 %). Please note that 3 to 8 W m^{-2} can be explained by the spectral range of BSRN measurements being less than for Heliosat-4 results. The bias is 12–13 W m^{-2} for the two northernmost sites and 2–12 W m^{-2} for stations in desert and semi-arid climates. The bias is greater for the other stations. The relative bias in KT is fairly similar for all stations: from 0 % to 6 %, with exception of Cabauw, Camborne, Palaiseau and Payerne. Biases for D (Table 4) are positive, from 31 to 49 W m^{-2}, except Izana (−6 W m^{-2}) and Tamanrasset (−14 W m^{-2}). This overestimation is greater than 25 % in relative values, except for Izana (−6 %) and Tamanrasset (−8 %). On the contrary, biases for B_N (Table 6) are negative in most cases, which contribute to overall small bias in G. The B_N bias is less than −55 W m^{-2} in most cases but reaches up to −163 W m^{-2} at Toravere. The large biases for B_N are observed at the two northernmost stations and we assume that they are a result of the large satellite viewing angles and eventually parallax effects as discussed in a next section. Both Izana and Tamanrasset are mountain stations in very specific environments. Consequently they unsurprisingly produce positive biases being different from the other stations (8 and 50 W m^{-2}.

The RMSE for G (Table 2) is between 74 and 94 W m^{-2} for all stations. It is fairly constant and as a

Table 6: Comparison between 15 min means of B_N measured and estimated by Heliosat-4.

Station	Number of samples	Mean observed value W/m^2	Bias W/m^2 (%)	RMSE W/m^2 (%)	Correlation coefficient
Lerwick	20980	296	−119 (−40 %)	250 (85 %)	0.665
Toravere	81000	457	−163 (−36 %)	288 (63 %)	0.718
Lindenberg	31006	399	−74 (−19 %)	205 (51 %)	0.799
Cabauw	89863	361	−35 (−10 %)	192 (53 %)	0.780
Camborne	29952	378	−22 (−6 %)	198 (52 %)	0.797
Palaiseau	74702	394	−45 (−11 %)	193 (49 %)	0.808
Payerne	65140	483	−32 (−7 %)	200 (41 %)	0.819
Carpentras	130201	560	−29 (−5 %)	160 (29 %)	0.873
Cener	42709	494	−55 (−11 %)	196 (40 %)	0.840
Sede Boqer	117485	620	−99 (−16 %)	235 (38 %)	0.770
Izana	76654	811	8 (1 %)	241 (30 %)	0.711
Tamanrasset	144591	599	50 (8 %)	208 (35 %)	0.816
De Aar	9654	730	−46 (−6 %)	190 (26 %)	0.862

Table 7: Comparison between 15 min means of Kt_{BN} measured and estimated by Heliosat-4.

Station	Number of samples	Mean observed value	Bias (%)	RMSE (%)	Correlation coefficient
Lerwick	20980	0.65	−0.359 (−56 %)	0.737 (114 %)	0.333
Toravere	81000	1.01	−0.485 (−48 %)	0.933 (92 %)	0.366
Lindenberg	31006	0.77	−0.205 (−27 %)	0.575 (74 %)	0.613
Cabauw	89863	0.70	−0.135 (−19 %)	0.522 (75 %)	0.605
Camborne	29952	0.69	−0.100 (−15 %)	0.496 (72 %)	0.650
Palaiseau	74702	0.74	−0.142 (−19 %)	0.538 (73 %)	0.628
Payerne	65140	0.81	−0.086 (−11 %)	0.509 (63 %)	0.633
Carpentras	130201	0.99	−0.095 (−10 %)	0.501 (51 %)	0.704
Cener	42709	0.84	−0.139 (−17 %)	0.498 (59 %)	0.693
Sede Boqer	117485	0.84	−0.184 (−22 %)	0.474 (56 %)	0.467
Izana	76654	1.43	−0.076 (−5 %)	1.012 (71 %)	0.598
Tamanrasset	144591	0.90	0.033 (4 %)	0.531 (59 %)	0.655
De Aar	9654	1.32	−0.261 (−20 %)	0.931 (71 %)	0.481

consequence, the relative RMSE decreases as the mean of the measurements of G increases, from 43 % for the northernmost station to 16 % for the stations exhibiting the largest mean SSI. A similar trend appears in KT. The RMSE for D (Table 4) is between 71 and 92 W m^{-2} for all stations. Because the mean D is fairly similar for all stations, the relative RMSE for D is quite stable around 55 % with exceptions such as Toravere (89 %), Izana (83 %) and De Aar (74 %). The range of RMSE for B_N (Table 6) is limited with values ranging mostly between 190 and 250 W m^{-2}. Like for G, the relative RMSE decreases as the mean of the observed B_N increases, from 85 % for the northernmost station to 30 % for the stations exhibiting the largest mean B_N.

One should note that the statistical quantities slightly vary from one year to another. As a whole, no clear trend was observed neither for year nor for month. However, it appears that in Europe, results are usually better for the summer months than for winter.

Lefèvre et al. (2013) found that in cloud-free conditions, the bias and RMSE in G_c, D_c and B_{cN} vary with θ_S though no clear trend appears. In all sky conditions, the bias and RMSE in G and D show a tendency to decrease as θ_S increases. This is in line with the decrease of G and D as θ_S increases. Sede Boqer and to a lesser extent Izana, Tamanrasset and De Aar do not exhibit such marked trends which are more obvious for Cabauw, Camborne, and Palaiseau. One may observe for the sites of Palaiseau and Payerne also studied in Lefèvre et al. (2013), a tendency of the bias in cloud-free conditions to decrease as θ_S increases for $\theta_S > 30\,°$. Accordingly, were the bias in K_c constant with θ_S, the bias on G would decrease with θ_S. As θ_S increases, the relative bias decreases while the relative RMSE increases. The situation is more confused for B_N in line with the findings of Lefèvre et al. (2013) for McClear since the cases for which B_N is noticeable are mostly cloud-free cases. It is possible that trends with θ_S and season exist but are possibly hidden by the larger inaccuracies on SSI induced by inaccuracies in the available aerosol and cloud properties.

8 Discussion

In this section, the influence of sky conditions on the errors is discussed in more detail in order to address the nowadays restrictions of Heliosat-4 and possible future improvements.

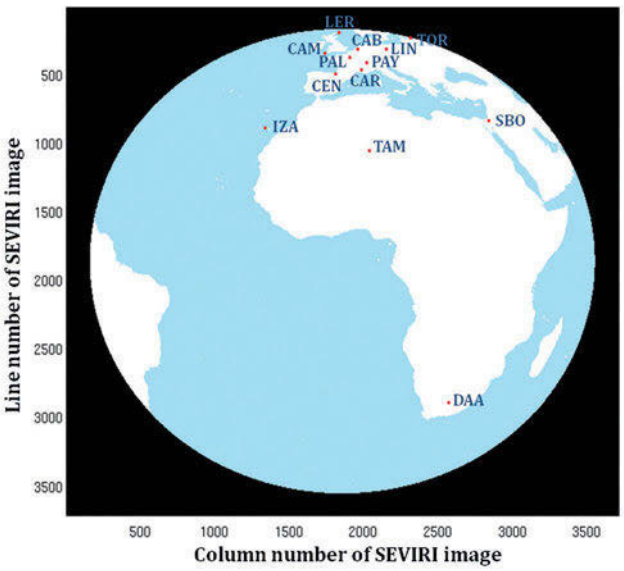

Figure 4: Valid domain of the cloud retrieval scheme APOLLO and the location of the 13 validated BSRN stations with satellite viewing angle below 72.5 °.

8.1 Satellite viewing angles greater than 60 °

In Tables 2–5, the two northernmost stations, Lerwick and Toravere, exhibit bias and RMSE for B_N that are greater than most of the other stations together with lower correlation coefficients. Degradation of the quality in the retrieval of cloud properties is caused by large satellite viewing angles. With latitudes approximately equal to 60 °, Lerwick and Toravere are nearly on the edge of the field of view of the MSG, and on the very edge of the valid domain of the cloud retrieval scheme APOLLO/SEV (Figure 4). The quality of estimates of cloud properties is low for these two stations, especially when the sun is low above horizon, e.g. in wintertime, or in early morning and late afternoon. Also, the plane-parallel approximation of radiative transfer is not valid anymore. Nevertheless, it has been decided to provide the data in those regions even if large biases are to be expected as several users have applications where the drawbacks are acceptable.

Analysis of individual data in Toravere also reveals that the bias of $-163\,\mathrm{W\,m^{-2}}$ for B_N is partly due to the presence of snow on the ground. APOLLO/SEV generally provides a discrimination of clouds and snow. But in those regions at the edge of the valid satellite viewing angle and in low sun conditions, snow is not detected in several cases and mistaken as clouds.

For sites far off the nadir of the satellite, i.e. with large viewing angles, and also in low sun elevation above horizon, errors due to the parallax effect become important (Schutgens and Roebeling, 2009). The parallax effect shifts the clouds actually covering these sites northwards (in the northern hemisphere) and the sensor aboard the satellite does not see the actual atmospheric conditions along the exact optical path between the sun and the station of interest. Additionally, the cloud is seen from the side which contrasts with the plane-parallel assumption made. This also contributes to the deviation between Heliosat-4 and ground measurements. Marie-Joseph et al. (2013) studied the retrieval of SSI using MSG images over French Guiana. This area exhibits similarities with the two stations in northern Europe as it is also located on the edge of the field of view of MSG. These authors found that the effect of the parallax on SSI or clearness index is more pronounced when the cloud cover is fragmented, i.e. when the spatial variability in the cloud cover is large. The effects are more pronounced on B_N than on G. For the latter a deficit in B_N can be partly balanced by an increase of the diffuse part D.

8.2 Underestimation of aerosol optical depth in the presence of desert dust aerosol

The bias in B_N (Table 6) for Tamanrasset is strongly positive ($+50\,\mathrm{W\,m^{-2}}$) in contrast to the other stations which exhibit negative or small positive biases for B_N. The sources of this overestimation of B_N reflect the difficulty in the estimation of the AOD by CAMS in desert regions, especially during desert dust events (Eskes et al., 2014a, 2014b). The data from the Aerosol Robotic Network (AERONET, Holben et al., 1998), which is an international network of ground stations monitoring aerosol optical depth and other aspects of atmospheric composition by means of sun photometers, are used as the observation reference. We analysed several case studies at Tamanrasset and found that the AOD at 550 nm is frequently underestimated by CAMS during the summer dust events. The AERONET daily mean data (blue line in Figure 5) exhibit AOD greater than 1, while CAMS failed to produce similar values. In such cases, the estimated direct irradiance is strongly overestimated.

The upper sub-plot in Fig. 6 exhibits a daily profile of B_N measured at Tamanrasset. Cloud-free conditions prevailed in the early morning and Heliosat-4 estimates, McClear estimates and measured B_N are very close to each other. At approximately 11:00 UT, B_N drops dramatically, signalling the arrival of the dust plume. This is confirmed with the corresponding increase of the AOD measured by AERONET (middle sub-plot, labelled AOD) and by the visual inspection of available MODIS images.

However, the same sub-plot shows that the AOD estimated by CAMS does not follow the same trend. It remains constant throughout the day, demonstrating that the CAMS model failed in representing the dust event in the level of detail being required for $B_N$modelling. CAMS AODs are given on nodes of a 1.125 ° longitude/latitude grid (about 125 km for Tamanrasset). Also, Tamanrasset is located on a steep slope of the mountains and next to a major dust source. Therefore, any spatial average as provided by atmospheric modelling on the global scale is most likely less accurate than in other re-

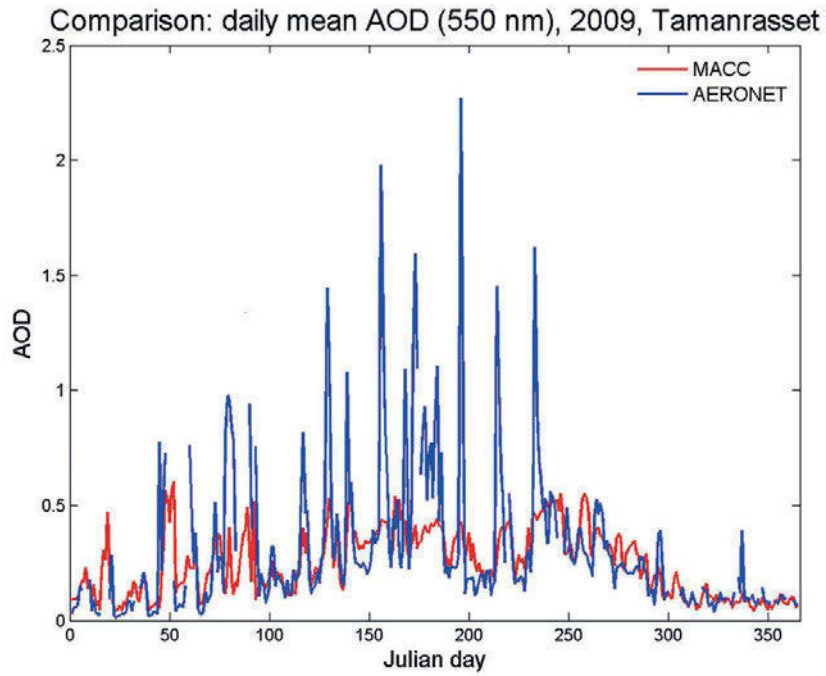

Figure 5: Daily mean AOD at 550 nm from CAMS (MACC)(red line) and AERONET (blue line, level 1.5 data, calculated from 500 nm data) for Tamanrasset, in 2009.

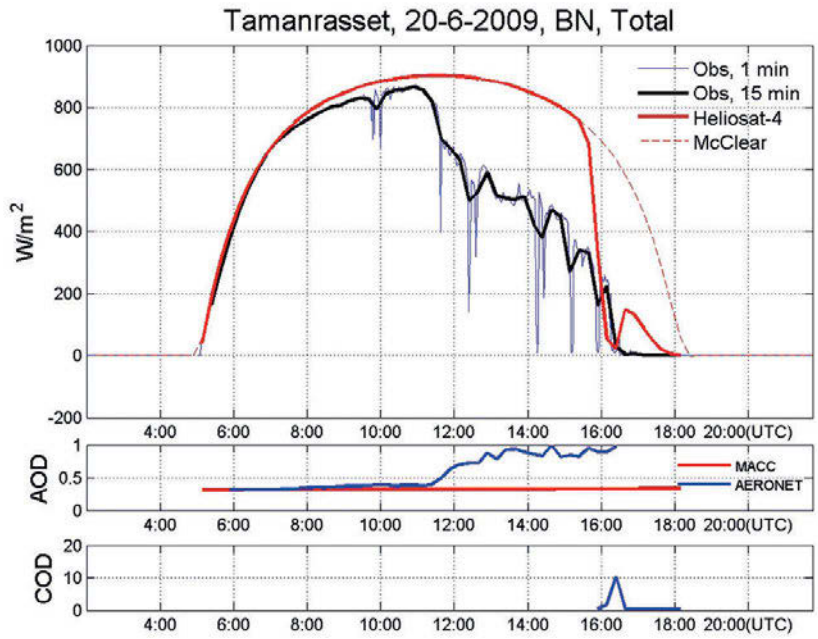

Figure 6: Upper graph: daily profile of B_N at Tamanrasset, 20 June 2009, from BSRN observations (thin blue line – 1 min data, black solid line – mean 15 min data), Heliosat-4 estimates (red solid line) and McClear estimates for clear sky (red dashed line, identical to Heliosat-4 estimation when clear sky, e.g. no cloud data from APOLLO/SEV); middle graph: the corresponding AOD from CAMS (MACC) (550 nm) and AERONET (550 nm, calculated from 500 nm data); lower graph: the corresponding cloud optical depth from APOLLO/SEV (no visible line in clear sky).

gions. But due to missing alternative validation stations in desert regions so far this assessment is provided here. As a consequence, Heliosat-4 overestimates B_N for the most of the day.

From the observation of BSRN and AERONET data, we found that this case with high aerosol loads in Tamanrasset lasted from 20 June 2009 to early July. During most of this period, the AOD is largely underestimated by CAMS. Therefore, this situation strongly contributes to the positive bias in estimates of B_N by Heliosat-4 in Tamanrasset. Dust events in Tamanrasset are frequent (Banks and Brindley, 2013), at least one

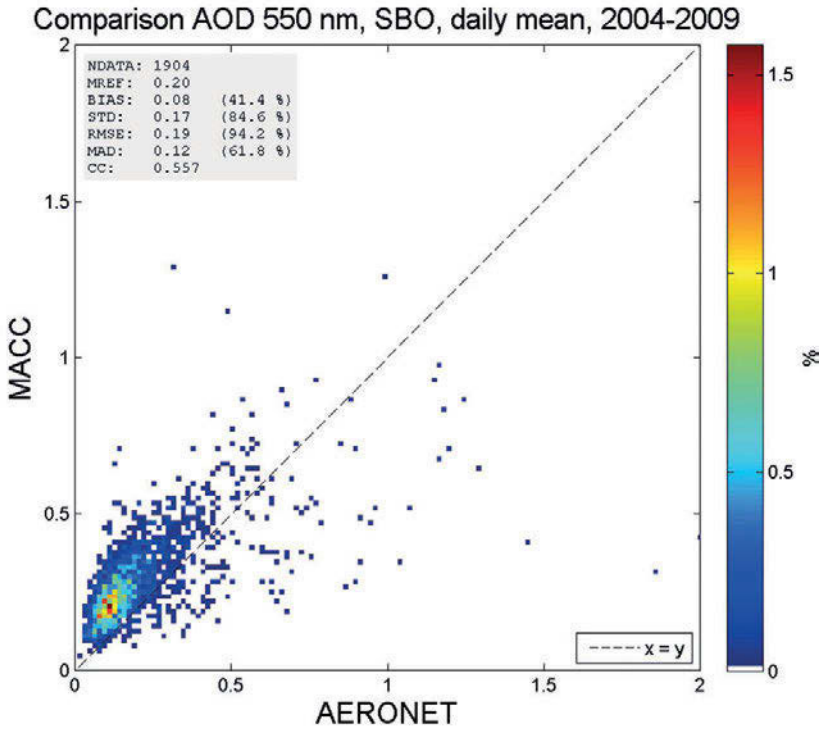

Figure 7: 2-D histogram between AERONET (level 1.5 data, calculated from 500 nm data) and CAMS (MACC) daily mean of AOD at 550 nm for Sede Boqer, 2004–2009.

per month in summer with different durations from a few hours to more than 10 days.

Similar situations were observed in other arid locations, such as Sede Boqer and De Aar, though the impact on Tamanrasset is more significant due to the intensity and frequency of the dust events.

8.3 Systematic overestimation of aerosol optical depth

Opposite to the underestimation of the AOD during dust events, we observed a systematic overestimation of AOD during periods without large dust loads for the desert stations Sede Boqer and Tamanrasset. Fig. 7 exhibits a 2-D histogram of the daily mean of AOD measured by AERONET and estimated by CAMS for 2004 to 2009. One observes an overestimation by CAMS, whose relative value is 41 % and concerns mainly low AOD cases (AOD < 0.5). These cases are the most frequent in Sede Boqer and this frequent overestimation of the AOD yields an overall underestimation of B_N by Heliosat-4 with a bias of $-99\,\mathrm{W\,m^{-2}}$ (Table 6). There are cases of large AERONET AOD which denote dust events being underestimated by CAMS. Frequent overestimation of small AOD values by CAMS is found (Fig. 5). This is masked by the frequent underestimation of the AOD in large AOD cases. Overall the bias is positive in Tamanrasset.

8.4 Cloud detection

It has been observed that clear-sky instants in early morning or late afternoon in winter at Sede Boqer are sometimes mistaken as clouds. A desert pixel may be seen as cold in the thermal and bright in the visible channels and therefore, it may be misinterpreted as cloud. One can observe this false alarm in Fig. 8 for the periods 5:00–9:00 UTC and 12:30–15:00 UTC during a winter day. The observed B_N are very close to the McClear estimates. This suggests that these instants are likely in cloud-free conditions as confirmed by the color composite MODIS images taken around 8:40 UTC of the same day. In contrast, all these instants are seen as cloudy by APOLLO/SEV (lower sub-plot), resulting in very low estimated B_N by Heliosat-4. Such situations contribute to the negative bias of B_N for the station Sede Boqer. If clear-sky instants only are retained for validation by using the filters in Lefèvre et al. (2013), the bias of Sede Boqer is $-68\,\mathrm{W\,m^{-2}}$ (−8 %), whereas it is $-99\,\mathrm{W\,m^{-2}}$ (−16 %) in all sky conditions (Table 6). The amplification of the negative bias may be partly explained by such false alarms in detection of clouds in winter conditions.

For all stations, rapid changes in cloud cover can be noticed in ground measurements, especially at 1 min sampling step. The spatial heterogeneity resulting from this patchwork of scattered clouds may induce a characterisation as cloud free by APOLLO/SEV because of the spatial integration effect.

Fig. 9 shows an example encountered in Carpentras during the summer of 2007. The strong temporal variation of the BSRN observations of B_N (thin blue line in upper sub-plot) around 14:00 UT indicates the presence of scattered/broken cloud. These clouds are detected by APOLLO/SEV as shown in the lower sub-plot (labeled

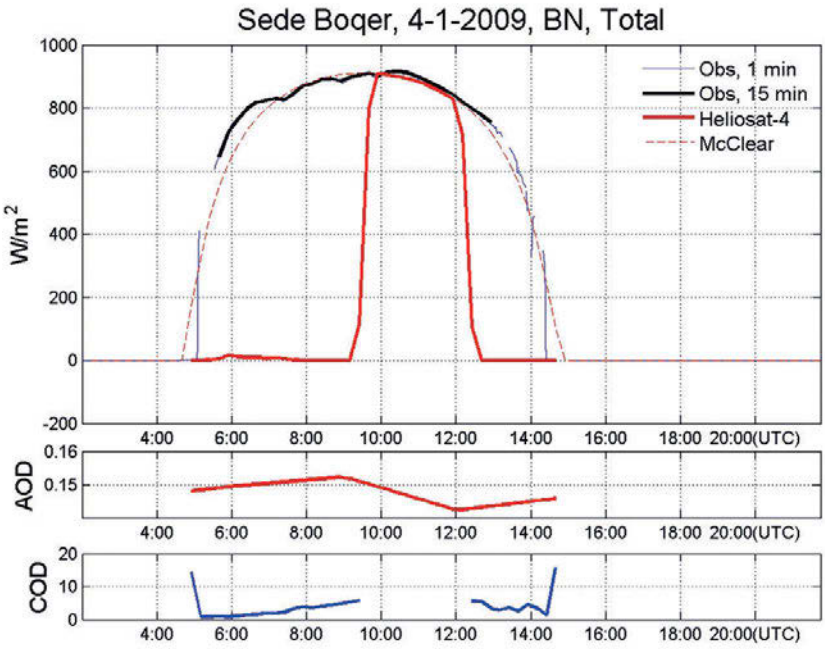

Figure 8: Upper graph: daily profile of B_N at Sede Boqer, 4 January 2009, from BSRN observations (thin blue line – 1 min data, black solid line – mean 15 min data), Heliosat-4 estimates (red solid line) and McClear estimates for clear sky (red dashed line, identical to Heliosat-4 estimates when clear sky, e.g. no cloud data from APOLLO/SEV); middle graph: the corresponding AOD from CAMS (MACC) (550 nm); lower graph: the corresponding cloud optical depth from APOLLO/SEV (no visible line in clear sky).

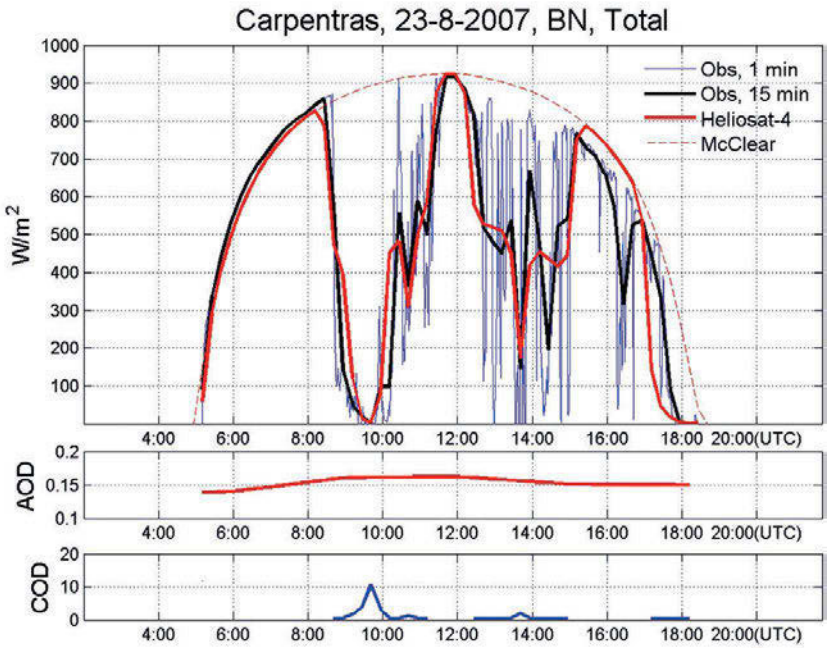

Figure 9: Upper graph: daily profile of B_N at Carpentras, 23 August 2007, from BSRN observations (thin blue line – 1 min data, black solid line – mean 15 min data), Heliosat-4 estimates (red solid line) and McClear estimates for clear sky (red dashed line, identical to Heliosat-4 estimates when clear sky, e.g. no cloud data from APOLLO/SEV); middle graph: the corresponding AOD from CAMS (MACC) (550 nm); lower graph: the corresponding COD from APOLLO/SEV (no visible line in clear sky).

COD) with relatively low cloud optical depth. Heliosat-4 estimates of 15-min mean B_N are close to the BSRN observations in this cloudy period. In the morning of the same day around 10:00 UT, the BSRN observations exhibit very low B_N with weak temporal variation at 1 min scale. This suggests that the cloud is optically thick and the sky is overcast. The Heliosat-4 estimates for this morning cloudy period are very close to the BSRN observations. Generally speaking, the values of B_N are well estimated throughout the day and the scattered/broken

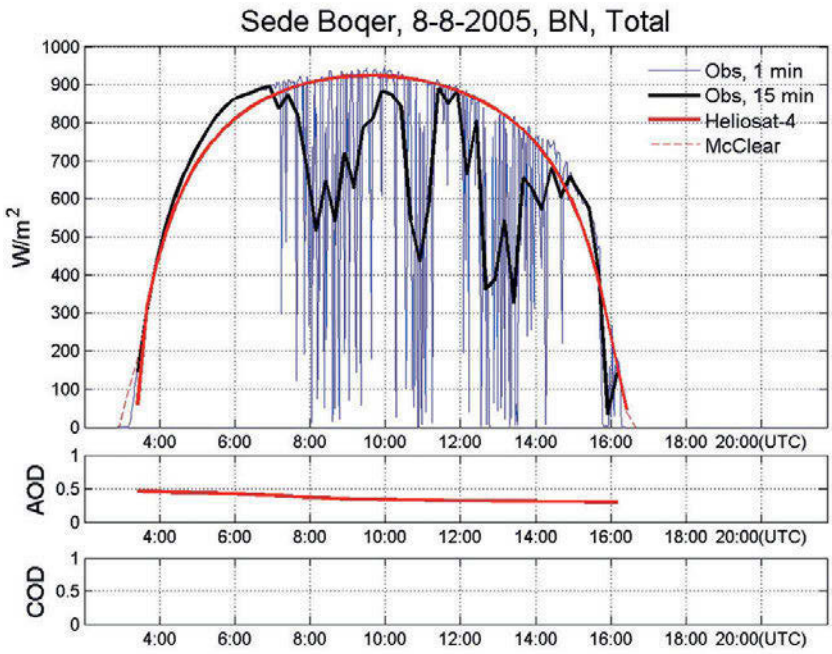

Figure 10: Upper graph: daily profile of B_N at Sede Boqer, 8 August 2005, from BSRN observations (thin blue line – 1 min data, black solid line – mean 15 min data), Heliosat-4 estimates (red solid line) and McClear estimates for clear sky (red dashed line, identical to Heliosat-4 estimates when clear sky, e.g. no cloud data from APOLLO/SEV); middle graph: the corresponding AOD from CAMS (MACC) (550 nm); lower graph: the corresponding COD from APOLLO/SEV (clear sky, no visible line in this case).

clouds presented in the afternoon around 14:00 UT are well detected in this example.

Figure 10 shows another example encountered in summertime in Sede Boqer. The very strong temporal variation of the BSRN observations of B_N suggests the presence of scattered clouds. On the opposite, the lower sub-plot (labelled COD) shows that according to APOLLO/SEV data, it was a cloud-free day. As a consequence, Heliosat-4 predicts clear sky irradiance and therefore overestimates B_N. Visual interpretation of a colour composite MODIS image centred on Sede Boqer around 09:10 UT indicates small-size cumulus in the northern region (Fig. 11). Sede Boqer is at the edge of the cloudy zone and it is hard to tell if its sky were cloudy or not at this very instant. Nevertheless, it supports the fact that rapid variations in B_N observed in BSRN data may result from this field of clouds. At this location, the SEVIRI sensor has a spatial resolution which is approximately 5 km, i.e. 10 times less than that of MODIS. It is difficult with such a coarse resolution to correctly detect these small cumulus clouds and retrieve their properties, especially in this desert region with high surface reflectance, contrarily to the previous example with predominantly cropland near Carpentras, and sub-pixel cloud shadows on the ground.

Figure 11: Color composite MODIS image (pixel size is 500 m) centred on Sede Boqer (blue circle) around 09:10 UTC on 8 August 2005.

8.5 Cloud-free cases

The bias in G is positive for all stations and ranges from 2 to 29 W m^{-2}. One cause of this overestimation is the difference between the total SSI and the SSI for the limited spectral bandwidth of the instruments as already discussed (Section 6). Another cause of this positive bias may originate from the McClear model and its inputs. Using the clear-sky subset of BSRN observations and comparing to McClear outputs –and not Heliosat-4 outputs,– an overestimation in G_c, ranging from 4 to 24 W m^{-2}, is observed for all sites, with the ex-

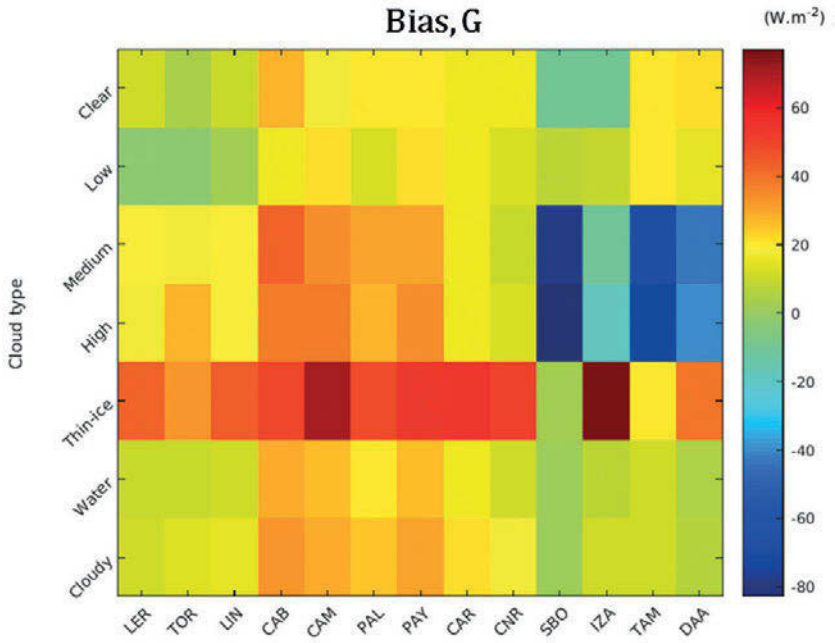

Figure 12: Bias in *G* for each station for several classes: clear (pixel is clear according to the APOLLO/SEV scheme), low (water cloud at low altitude), medium (water/mixed phase cloud at medium altitude), high (water/mixed phase cloud of large vertical extent), thin-ice (thin ice cloud), water (cloud is treated as a water cloud), cloudy (pixel is cloudy).

ception of Lerwick ($-21\,\mathrm{W\,m^{-2}}$) and Izana ($-5\,\mathrm{W\,m^{-2}}$). These findings are in line with those of Lefèvre et al. (2013) for the five sites common to their study and ours: Palaiseau, Payerne, Carpentras, Sede Boqer, Tamanrasset, for slightly different periods. Therefore, McClear tends to introduce a positive bias in the estimation of *G* from Heliosat-4. The RMSE ranges between 18 and $30\,\mathrm{W\,m^{-2}}$. For each station, it is far less than the RMSE observed in all sky conditions (Table 2), and also, greater correlation coefficients are found.

Comparing Heliosat-4 outputs to the same clear-sky subset of BSRN leads to similar biases, RMSE and correlation coefficients as for McClear with a few exceptions. At Lerwick, the underestimation is enhanced (from -21 down to $-26\,\mathrm{W\,m^{-2}}$) likely because of the low quality of cloud properties retrieval for this site at the edge of field of view of MSG, several cloud-free instants are mistaken as cloudy. The RMSE increases from 26 to $33\,\mathrm{W\,m^{-2}}$, and the correlation coefficient slightly decreases from 0.987 down to 0.979. On the other hand, and for the same reasons that act favourably in this case, Toravere exhibits a decrease in bias, from 12 to $4\,\mathrm{W\,m^{-2}}$. However, the RMSE increases from 20 to $28\,\mathrm{W\,m^{-2}}$, and the correlation coefficient decreases from 0.992 down to 0.982. The case of Sede Boqer has been discussed and results in an increase of the RMSE, from 27 up to $37\,\mathrm{W\,m^{-2}}$, with a decrease of the correlation coefficient (0.988 and 0.972). Izana exhibits similar behaviour: change of RMSE from 19 up to $35\,\mathrm{W\,m^{-2}}$, and change in correlation coefficient from 0.995 down to 0.984.

8.6 Cloud coverage and cloud optical depth

Other causes of error are related to the clouds and their properties. Fig. 12 displays the bias in *G* for each station for several classes: clear (pixel is clear according to the APOLLO/SEV scheme), low (water cloud at low altitude), medium (water/mixed phase cloud at medium altitude), high (water/mixed phase cloud of large vertical extent), thin-ice (thin ice cloud), water (cloud is treated as a water cloud) and cloudy (pixel is cloudy).

The bias observed for the clear cases as defined by APOLLO/SEV ranges between 13 and $25\,\mathrm{W\,m^{-2}}$ for all stations with the exception of Cabauw (37), Camborne (34) and Payerne (32). It is always positive and contributes to the overall overestimation for all sky conditions.

For the APOLLO/SEV clear cases, the RMSE is greater than that observed for the clear-sky BSRN subset by a factor of more than 2. Most probably these are scattered clouds being treated as partly cloudy pixels in the spatial range of MSG and also providing a large variability of SSI.

The RMSE is much less than that for all sky conditions for all southernmost stations: Carpentras, Cener, Sede Boqer, Izana, Tamanrasset, De Aar, which experience frequent clear skies. It ranges from 56 to $84\,\mathrm{W\,m^{-2}}$ for the clear cases and from 74 to $94\,\mathrm{W\,m^{-2}}$ for all sky conditions. On the other hand, the RMSE is similar or even greater than that for all sky conditions for the other stations where cloudy skies are more frequent and cloud-free cases are less frequent. This increasing

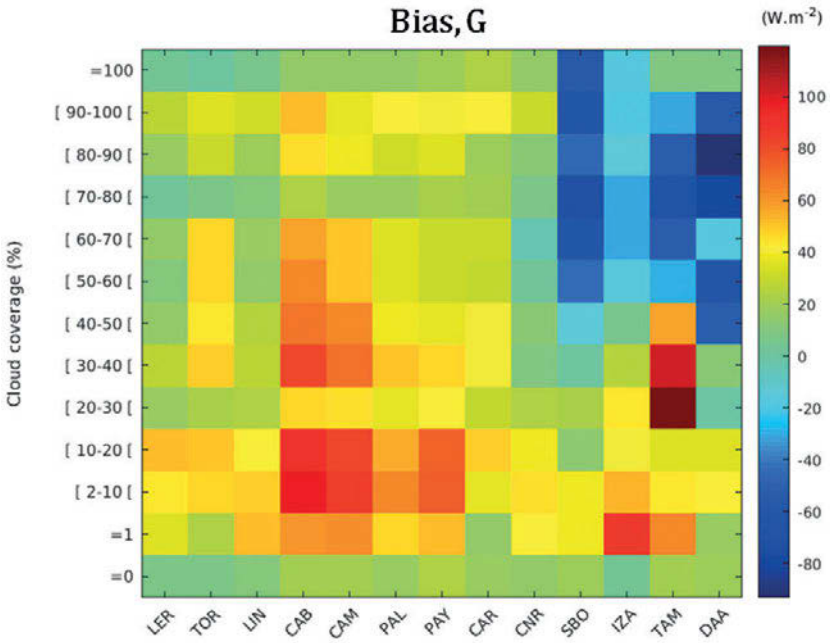

Figure 13: Bias in G for each station as a function of the cloud coverage.

RMSE in more cloudy conditions again raises the point to investigate the treatment of partly cloudy pixels further on.

As a whole, the bias is rarely negative and most of the situations exhibit overestimation in G. One exception is that the cases of medium and high clouds for the desert stations exhibit large negative bias. However, the number of sample of these cases is quite small as these cloudy situations are not encountered very often.

The bias for the case of thin ice cloud is large compared to the other cases. Thin ice clouds are typically semi-transparent and the retrieval of COD is highly unsure as the ice particles show a large variety of geometrical shapes and sizes. Any assumption on optical properties is therefore highly uncertain. Also, the influence of ground reflectances is increased, and the chosen 2-stream approach in the APOLLO reflectance to COD parameterization is restricted in such small COD cases. Overall, the current treatment of thin ice clouds results in an underestimation of τ_{cloud} which in turn yields an overestimation in G in all stations except Sede Boqer.

Fig. 13 exhibits the bias in G for each station as a function of the cloud coverage estimated by the APOLLO/SEV scheme. The row (0 %) corresponds to the row "clear" in Fig. 12. One may observe that the bias varies with the cloud coverage for the same station and from station to station for the same cloud coverage. As a whole, most of the situations exhibit overestimation in G. Except for a few sites, the bias is positive and small when the sky is clear (0 %) or fully covered (100 %). The greatest positive biases are found for cloud coverage less than 20 %, and especially for the classes between 2 % and 10 %. They may be greater than 60 W m^{-2}. Heliosat-4 and the APOLLO/SEV must be improved for small cloud coverages as these cases are frequently met. Cabauw and Camborne, and to a lesser extent Palaiseau and Payerne, exhibit similar structures with a small bias for coverage of 0 % and 100 % and large biases otherwise. Stations in desert, semi-arid, and Mediterranean climates exhibit large underestimation for partial coverage greater than 50 %. In addition, Tamanrasset offers large overestimation for small coverage. It should be noted that the number of these partly covered cases is low for these stations where cloud-free conditions prevail.

Fig. 14 shows the RMSE in G for each station as a function of the cloud coverage. One may observe that the RMSE for clear sky (0 %) is fairly low and similar for all stations: it ranges from 56 (Carpentras) to 104 W m^{-2} (Lerwick). It is smallest for the stations in desert, semi-arid, and Mediterranean climates which experience frequent clear skies. The RMSE exhibits similar values for overcast skies (cloud coverage = 100 %) for the stations in the marine climate and that these values are close to the RMSE observed for clear skies (last row in Fig. 14) though slightly greater. In contrast, the RMSE for stations in desert, semi-arid, and Mediterranean climates is greater than those for the other stations.

Large RMSEs are encountered for partly covered cases. The greatest RMSEs are found for the desert stations for partly covered cases; however, their frequency is small and hence their impact is low. These errors for partly covered instants originate from multiple sources, amongst them parallax effects, cloud detection, the estimation of cloud coverage and τ_{cloud} as previously discussed.

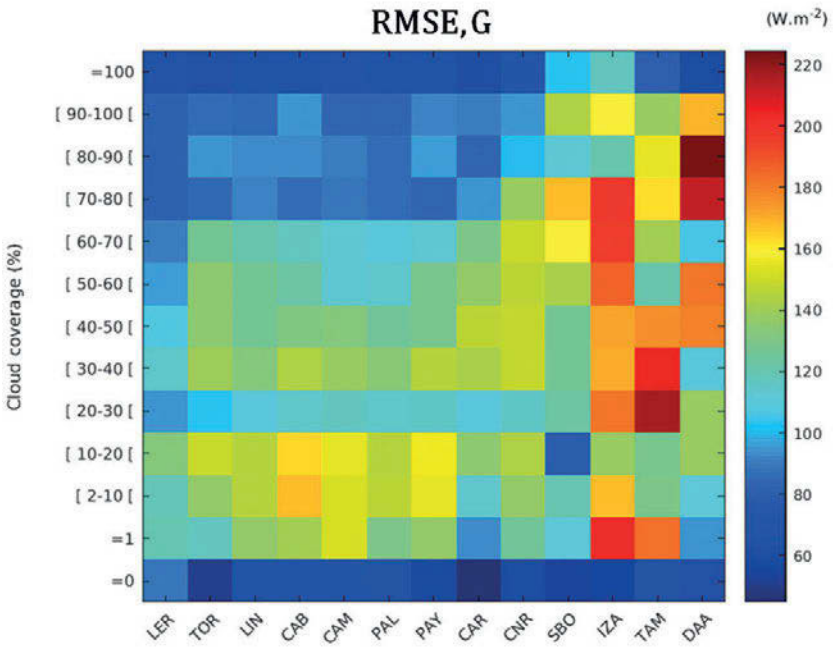

Figure 14: RMSE in G for each station as a function of the cloud coverage.

8.7 Cloud phase

Uncertainties in the estimation of the cloud phase are another source for overestimation in G. The cloud phase has a significant influence on the estimation of G. Typically, ice clouds scatter the light more than water clouds and the amount of light scattered downward is less for ice clouds. Greuell et al. (2013) reported that on the average thick ice clouds are optically thicker than water clouds and KT_B, and KT_{BN} decreases more sharply as τ_{cloud} increases. In the current Heliosat-4 implementation, low, medium and high clouds as detected by APOLLO/SEV are considered as water clouds and only the thin ice cloud is treated as an ice cloud. This is known to be an oversimplification in remote sensing as medium and high clouds as detected in APOLLO/SEV are often mixed phase clouds with ice particles in their upper parts. Considering deep, high reaching clouds as pure water clouds tends to falsely decrease the scattering and overestimate G. This can be seen in Fig. 13 for the northern sites. Additional tests made with libRadtran when assuming that the high clouds are made of two phases yield a strong decrease of the bias by a factor of 2–3 for the northern sites. It could be recommended that future versions of Heliosat-4 include such a revised treatment of high and medium level clouds as detected in APOLLO/SEV.

8.8 Influence of the circumsolar irradiance

There are several definitions of the direct normal irradiance B_N (Blanc et al., 2014a). Ground-based measurements made by pyrheliometers oriented towards the sun typically have an aperture half-angle of approximately 2.5 °. These instruments collect part of the radiation coming from the circumsolar region. On the contrary, B_N estimated by radiative transfer models – as is the case of Heliosat-4 – is valid for a sun being considered as a point source. The difference between the two is defined as the circumsolar irradiance (Blanc et al., 2014a). In clear-sky conditions, the intensity of circumsolar irradiance is less than 10 W m^{-2} in most cases (Oumbe et al., 2012) and is fairly similar to the uncertainty of the instruments. In cloudy-sky conditions or heavy aerosol conditions, the relative contribution of the circumsolar irradiance to B_N measured by pyrheliometers may exceed 50 % due to specific effects of especially cirrus clouds. This explains a large part of the negative bias of B_N and KT_{BN} presented in the Tables 6 and 7.

It is desirable to bring a correction to K_{cB} estimated by Heliosat-4 when comparing to ground measurements. Building on the work of Shiobara and Asano (1993) and Reinhardt et al. (2012), Qu (2013) has proposed an empirical correction applying to K_{cB} when the cloud coverage of a pixel is greater than or equal to 50 % by multiplying τ_{cloud} in Eq. (4.1) by 0.45 for thin ice clouds and 0.75 for all other cloud types. He found a reduction in bias for B_N and KT_{BN}. Though promising, the study was of limited extension and more work is needed on the applicability of this correction and its integration in Heliosat-4.

8.9 Overestimation of the diffuse irradiance

D is generally overestimated by Heliosat-4 by about 30 W m^{-2} for the northern stations with marine climate (Table 4). For the desert/semi-arid stations such as Tamanrasset and Izana, due to the occasionally underestimations of the aerosols loads during the dust storms,

the biases in D are negative for these two stations. For the other two desert stations, Sede Boqer and De Aar, where the presence of the dust storm is less frequent and less intense, the bias in D is positive.

As previously discussed, the estimates of D comprise the circumsolar irradiance which is included into the measurements of B_N. This explains partly the overestimation of D.

The cloud phase, particle form, size, and their distributions have influence in the modelling of the scattering of radiances. The same holds for the aerosols type, size and size distribution. However, the information concerning these properties is not sufficiently available. Approximations are made in the modelling concerning the cloud and aerosols. In our case, the sizes of the cloud water droplets and ice crystals are fixed due to limited information. Further, for the aerosols, the OPAC (Optical Properties of Aerosols and Clouds, Hess et al., 1998) aerosol profiles and aerosol types are used. These standard aerosol profiles offer a practical way to obtain an approximation of the real situation though they contain uncertainties. These are factors among others which may contribute to the errors in D. To fully understand the reason why there is a general overestimation of D, more efforts are still needed. This will help to further improve the performance of Heliosat-4 method.

9 Conclusions

The new Heliosat-4 method has been designed in the scope of being set up as an operational tool for solar irradiance monitoring in the framework of the MACC projects and the Copernicus programme. It exhibits satisfactory results as a fast implementation of radiative transfer theory for the direct and global irradiance for clear and cloudy skies. Furthermore, the use of radiative transfer principles instead of empirical relations allows the extension towards spectrally resolved irradiances in future and the use of enhanced cloud and aerosol information as soon as they will be available in future.

The comparison between Heliosat-4 estimates and measurements of global and beam SSI for 13 stations shows a large correlation coefficient at all stations. For 15 min averages of global SSI, it ranges between 0.91 and 0.97. This demonstrates that Heliosat-4 offers accurate estimates of changes in time of the global SSI every 15 min. The bias of global SSI ranges between 2 and 32 W m^{-2}. This study neglects the differences between spectral ranges of BSRN and Heliosat-4, accounting for a 3–8 W m^{-2} bias as known from sensitivity studies. The RMSE is between 74 and 94 W m^{-2} and its relative value ranges between 15 % and 20 % of the mean observed irradiance for stations in desert and Mediterranean climate, and between 26 % and 43 % for rainy climate with mild winters. The correlation coefficient for the diffuse irradiance ranges between 0.68 and 0.87. The bias is comprised between −14 and +49W m^{-2}, and the RMSE between 71 W m^{-2} (74 %) and 92 W m^{-2} (83 %). The correlation coefficient for the direct normal irradiance ranges between 0.67 and 0.87. The bias is comprised between −163 and +50 W m^{-2}, and the RMSE between 160 W m^{-2} (29 %) and 288 W m^{-2} (63 %).

The main novelty of the Heliosat-4 method is its design that *i)* is based on a fast approximation of the radiative transfer equation, and *ii)* is combining existing advanced models such as the McClear model for estimating the SSI under clear skies, cloud properties schemes such as APOLLO/SEV applied to images acquired by MSG, and aerosol optical properties, water vapour, and ozone provided by CAMS with an update frequency of 3 h on the global scale.

Performances are still far from WMO standards (WMO, 2008) which ask for a bias less than 3 W m^{-2} and 95 % of the deviations less than 20 W m^{-2}. The quality of the input parameters describing the state of the atmosphere in clear sky, the cloud properties and the ground reflectance is obviously a major influence on the performance of the Heliosat-4 method. Paths for improvements have been discussed.

The quality of the results of Heliosat-4 depends on the site and especially of its climate. Large satellite viewing angles may decrease the quality of the estimation. Snow cover may pose a problem because even in the used snow/cloud discrimination scheme, snow can still be mistaken as cloud.

Scattered or broken clouds are difficult to detect because of the complex and changing cloud structure and the limits of the spatial and temporal resolution of the SEVIRI sensor aboard MSG. Three-dimensional cloud effects as the parallax effect of clouds in low sun conditions or the overshooting of G due to reflection on the side of the cloud are not treated due to missing cloud structure information in the daily operational practice. The spatial heterogeneity resulting from this patchwork of small broken clouds may induce a false detection by APOLLO/SEV and actual cloudy cases are taken as clear cases thus yielding an overestimation of the global SSI.

The cloud masking and the retrieval of COD should be enhanced following the feedback given from the solar irradiance evaluation. This work is ongoing (Klüser et al., 2015) and APOLLO_NG (Next Generation) is making use of a probabilistic cloud masking and treats cloud effective radius explicitly. APOLLO_NG is currently evaluated with respect to Heliosat-4 irradiances and with respect to CREW (Cloud Retrieval Evaluation Workshop) datasets. If successful, APOLLO_NG will be implemented in Heliosat-4 and a major reprocessing of cloud properties is foreseen.

The retrieval of the cloud properties when a pixel is not fully covered by clouds should be improved. In case of clear sky, uncertainties in the retrieval of aerosol properties for desert stations become important.

The underestimation of the aerosol optical depth during dust events in or near desert regions may be significant. It introduces a strong positive bias for the estimation of the direct SSI. A systematic overestimation of

the aerosol optical depth in non-dust-storm periods for desert stations may cause an underestimation of the direct SSI.

Besides these improvements on the quality of the inputs, the Heliosat-4 model can be improved to better account for the vertically developed clouds by considering them as two-phase clouds. This could be done by computing additional abaci. A correction on circumsolar irradiance should be also applied when comparing to ground-based measurements which is expected to largely reduce the bias of D and B_N especially for cirrus clouds.

The Heliosat-4 method with inputs from CAMS, MODIS and APOLLO/SEV from DLR is available as a Web service, i.e. an application that can be invoked via the Web and using always the best-available input data and algorithm version. It obeys the OGC (Open Geospatial Consortium) standard for Web processing services (WPS, Percivall et al., 2011). An interface has been developed to launch Heliosat-4 within a standard Web browser and to obtain time-series of global, direct, diffuse and direct normal SSI for a given point and a given period from 2004 until 2 days before today. The summarization towards 1 min, 15 min, 1 h, 1 day, and 1 month sums is provided. This interface is called CAMS Radiation Service in this context and can be launched via the catalogue of CAMS products (www.copernicus-atmosphere.eu).

Acknowledgements

The research leading to these results has received funding from the European Union's Seventh Framework Programme (FP7/2007-2013) under Grant Agreement no. 218793 (MACC project) and no. 283576 (MACC-II project) and from the European Union's Horizon 2020 Programme (H2020/2014-2020) under grant agreement no. 633081 (MACC-III project). The MACC (Monitoring Atmospheric Composition and Climate) projects are preparatory projects for Europe's Copernicus programme. The authors thank all ground station operators of the BSRN network for their valuable measurements and the Alfred-Wegener Institute for hosting the BSRN website. The authors thank the team developing libRadtran (http://www.libradtran.org).

Appendix – List of symbols

Symbol	Description
G	Global surface solar irradiance received on a horizontal plane
G_c	Global surface irradiance for clear sky, i.e. cloudless sky, received on a horizontal plane
B	Beam/direct surface irradiance received on a horizontal plane
B_c	Beam/direct surface irradiance for clear sky received on a horizontal plane
B_N	Beam/direct surface irradiance received on a plane always normal to sun rays
D	Diffuse surface irradiance received on a horizontal plane
D_c	Diffuse surface irradiance for clear sky received on a horizontal plane
E_0	Irradiance received on a horizontal plane located at the top of atmosphere
KT	Clearness index
KT_B	Direct clearness index
KT_c	Clearness index for clear sky
KT_{Bc}	Direct clearness index for clear sky
KT_d	Diffuse clearness index
KT_{BN}	Direct normal clearness index
K_{cG}	Clear-sky index for global horizontal irradiance
K_{cB}	Clear-sky index for beam horizontal irradiance
θ_S	Solar zenithal angle
ρ_g	Ground albedo
ρ_{ws}	White sky albedo (bi-hemispherical reflectance)
ρ_{bs}	Black sky albedo (directional-hemispherical reflectance)
P_c	Clear sky properties (in our case clear sky and cloudless sky are used as synonyms)
P_{c0}	Typical values of the clear sky properties
P_{cloud}	Cloud properties
τ_{cloud}	Cloud optical depth
S_{cloud}	Cloud spherical albedo

References

Anderson, G.P., S.A. Clough, F.X. Kneizys, J.H. Chetwynd, E.P. Shettle, 1986: AFGLatmospheric constituent profiles (0–120 km). – Technical Report AFGL-TR-86-0110, AFGL(OPI), Hanscom AFB, MA. 01736.

Banks, J.R., H.E. Brindley, 2013: Evaluation of MSG-SEVIRI mineral dust retrieval products over North Africa and the Middle East. – Remote Sens. Env. **128**, 58–73, DOI: 10.1016/j.rse.2012.07.017.

Benedetti, A., J.W. Kaiser, J.-J. Morcrette, 2011: Global Climate. Aerosols [in "State of the Climate in 2010"]. – Bull. Amer. Meteor. Soc. **92**, S65-S67.

Beyer H.-G., C. Costanzo, D. Heinemann., 1996: Modifications of the Heliosat procedure for irradiance estimates from satellite images. – Solar Energy **56**, 207–212.

Blanc, P., L. Wald, 2012: The SG2 algorithm for a fast and accurate computation of the position of the Sun. – Solar Energy **86**, 3072–3083, DOI:10.1016/j.solener.2012.07.018.

Blanc, P., B. Gschwind, M. Lefèvre, L. Wald, 2011: The HelioClim project: Surface solar irradiance data for climate applications. – Remote Sens. **3**, 343–361, DOI: 10.3390/rs3020343.

Blanc, P., B. Espinar, N. Geuder, C. Gueymard, R. Meyer, R. Pitz-Paal, B. Reinhardt, D. Renne, M. Sengupta, L. Wald, S. Wilbert, 2014a: Direct normal irradiance related definitions and applications: the circumsolar issue. –Solar Energy **110**, 561–577, DOI:10.1016/j.solener.2014.10.001.

Blanc, P., B. Gschwind, M. Lefèvre, L. Wald, 2014b: Twelve monthly maps of ground albedo parameters derived from MODIS data sets. – In Proceedings of IGARSS 2014, held 13–18 July 2014, Quebec, Canada, USBKey, pp. 3270–3272. Data available at http://www.oie.mines-paristech.fr/Valorisation/Outils/AlbedoSol/

Calbó, J., D. Pagès, J.-A. González, 2005: Empirical studies of cloud effects on UV radiation: A review. – Rev. Geophys. **43**, RG2002, DOI:10.1029/2004RG000155.

Cano, D., J. Monget, M. Albuisson, H. Guillard, N. Regas, L. Wald, 1986: A method for the determination of the global solar radiation from meteorological satellite data. – Solar Energy **37**, 31–39.

Den Outer, P.N., H. Slaper, J. Kaurola, A. Lindfors, A. Kazantzidis, A.F. Bais, U. Feister, J. Junk, M. Janouch, W. Josefsson, 2010: Reconstructing of erythemal ultraviolet radiation levels in Europe for the past 4 decades. – J. Geophys. Res. **115**, D10102, DOI: 10.1029/2009JD012827.

Deneke, H.M., A.J. Feijt, R.A. Roebeling, 2008: Estimating surface solar irradiance from Meteosat SEVIRI-derived cloud properties. – Remote Sens. Env. **12**, 3131–3141.

Eissa, Y., S. Munawwar, A. Oumbe, P. Blanc, H. Ghedira, L. Wald, H. Bru, D. Goffe, 2015a: Validating surface downwelling solar irradiances estimated by the McClear model under cloud-free skies in the United Arab Emirates. – Solar Energy **114**, 17–31, DOI:10.1016/j.solener.2015.01.017.

Eissa, Y., M. Korany, Y. Aoun, M. Boraiy, M.A. Wahab, S. Alfaro, P. Blanc, M. El-Metwally, H. Ghedira, L. Wald, 2015b: Validation of the surface downwelling solar irradiance estimates of the HelioClim-3 database in Egypt. – Remote Sens. **7**, 9269–9291, DOI:10.3390/rs70709269.

Eskes, H.J., A. Benedictow, A.-M. Blechschmidt, I. Bouarar, E. Botek, S. Chabrillat, Y. Christophe, E. Cuevas, H. Clark, H. Flentje, A. Gaudel, J. Griesfeller, V. Huijnen, N. Huneeus, L. Jones, J. Kapsomenakis, E. Katragkou, S. Kinne, B. Langerock, K. Lefever, D. Melas, M. Razinger, A. Richter, M. Schulz, W. Thomas, V. Thouret, M. Vrekoussis, A. Wagner, C. Zerefos, 2014a: Validation Report of the MACC Reanalysisof Global Atmospheric Composition: Period 2003–2012. – MACC Report, 29 June 2014, available at: http://www.copernicus-atmosphere.eu/ (last access: 10 April 2016).

Eskes, H.J., T. Antonakaki, A. Arola, A. Benedictow, A. Blechschmidt, E. Botek, S. Chabrillat, Y. Christophe, E. Cuevas, H. Flentje, A. Gaudel, V. Huijnen, J. Kapsomenakis, S. Kinne, B. Langerok, M. Razinger, A. Richter, M. Schulz, V. Thouret, M. Vrekoussis, A. Wagner, C. Zerefos, 2014b: Validation Reportof the MACC Near-Real Time Global Atmospheric CompositionService: System Evolution and Performance Statistics, Status upto 1 June 2014. – MACC Report, 30 September 2014, available at: http://www.copernicus-atmosphere.eu/ (last access: 10 April 2016).

Farr, T.G., E. Caro, R. Crippen, R. Duren, S. Hensley, M. Kobrick, M. Paller, E. Rodriguez, P. Rosen, L. Roth, D. Seal, S. Shaffer, J. Shimada, J. Umland, M. Werner, 2007: The Shuttle Radar Topography Mission. – Rev. Geophys. **45**, RG2004, DOI:10.1029/2005RG000183.

Fu, Q., 1996: An accurate parameterization of the solar radiative properties of cirrus clouds for climate models. – J. Climate **9**, 2058–2082.

Fu, Q., P. Yang, W.B. Sun, 1998: An accurate parameterization of the infrared radiative properties of cirrus clouds for climate models – J. Climate **11**, 2223–2237.

Gesch, D.B., K.S. Larson, 1996: Techniques for development of global 1-kilometer digital elevation models. Human Interactions with the Environment-Perspectives from Space. –13th, Sioux Falls, South Dakota, August 20–22, 1996, Proceedings: Bethesda, Maryland, American Society of Photogrammetry and Remote Sensing.

Greuell, W., R. Roebeling, 2009: Toward a standard procedure for validation of satellite-derived cloud liquid water path: A study with SEVIRI data. – J. Appl. Meteor. Climatol. **48**, 1575–1590.

Greuell, W., J.F. Meirink, P. Wang, 2013: Retrieval and validation of global, direct, and diffuse irradiance derived from SEVIRI satellite observations. – J. Geophys. Res. Atmos. **118**, 2340–2361, DOI:10.1002/jgrd.50194.

Hess, M., P. Koepke, I. Schult, 1998: Optical properties of aerosols and clouds: The software package OPAC. B. – Amer. Meteor. Soc. **79**, 831–844.

Holben, B.N., T.F. Eck, I. Slutsker, D. Tanré, J.P. Buis, A. Setzer, E. Vermote, J.A. Reagan, Y. Kaufman, T. Nakajima, F. Lavenu, I. Jankowiak, A. Smirnov, 1998: AERONET – A federated instrument network and data archive for aerosol characterization. – Remote. Sens. Env. **66**, 1–16.

Huang, G.H., M.G. Ma, S.L. Liang, S.M. Liu, X. Li, 2011: A LUT-based approach to estimate surface solar irradiance by combining MODIS and MTSAT data. – J. Geophys. Res.–Atmos. **116**, D22201, DOI:10.1029/2011JD016120.

Kaiser, J.W., V.-H. Peuch, A. Benedetti, O. Boucher, R.J. Engelen, T. Holzer-Popp, J.-J. Morcrette, M.J. Wooster, MACC-II Management Board, 2012: The pre-operational GMES Atmospheric Service in MACC-II and its potential usage of Sentinel-3 observations. – ESA Special Publication SP-708, Proceedings of the 3rd MERIS/(A)ATSR and OCLI-SLSTR (Sentinel-3) Preparatory Workshop, held in ESA-ESRIN, Frascati, Italy, 15–19 October 2012.

Klüser, L., N. Killius, G. Gesell, 2015: APOLLO_NG – a probabilistic interpretation of the APOLLO legacy for AVHRR heritage channels, Atmos. Meas. Tech. **8**, 4155–4170, DOI:10.5194/amt-8-4155-2015.

Kriebel, K.T., R.W. Saunders, G. Gesell, 1989: Optical properties of clouds derived from fully cloudy AVHRR pixels. Beitr. Phys. Atmosph., **62**(3), 165–171.

Kriebel, K.T., G. Gesell, M. Kästnerc, H. Mannstein, 2003: The cloud analysis tool APOLLO: Improvements and validations, Int. J. Remote Sensing, **24**(12), 2389–2408, DOI:10.1080/01431160210163065.

Lefèvre, M., A. Oumbe, P. Blanc, B. Espinar, B. Gschwind, Z. Qu, L. Wald, M. Schroedter-Homscheidt, C. Hoyer-Klick, A. Arola, A. Benedetti, J.W. Kaiser, J.-J. Morcrette, 2013: McClear: a new model estimating downwelling solar radiation at ground level in clear-sky conditions. – Atmos. Meas. Tech. **6**, 2403–2418, DOI: 10.5194/amt-6-2403-2013.

Marie-Joseph, I., L. Linguet, M.-L. Gobinddass, L. Wald, 2013: On the applicability of the Heliosat-2 method to assess surface solar irradiance in the Intertropical Convergence Zone, French Guiana. Int. J. Remote Sens. **34**, 3012–3027, DOI: 10.1080/01431161.2012.756598.

Mayer, B., A. Kylling, 2005: Technical note: The libRadtran software package for radiative transfer calculations – description and examples of use. – Atmos. Chem. Phys. **5**, 1855–1877, DOI:10.5194/acp-5-1855-2005.

Mayer, B., A. Kylling, C. Emde, R. Buras, U. Hamann, 2010: libRadtran: library for radiative transfer calculations, Edition 1.0 for libRadtran version 1.5-beta. – http://www.libradtran.org, (accessed at 10 April 2013).

Möser, W., E. Raschke, 1984: Incident solar radiation over Europe estimated from Meteosat data. – J. Appl. Meteor. **23**, 166–170.

Mueller, R., C. Matsoukas, A. Gratzki, H. Behr, R. Hollmann, 2009: The CM-SAF operational scheme for the satellite based retrieval of solar surface irradiance – a LUT based eigenvector hybrid approach. – Remote Sens. Env. **113**, 1012–1024, DOI:10.1016/j.rse.2009.01.012.

Ohmura, A., H. Gilgen, H. Hegner, G. Mueller, M. Wild, E.G. Dutton, B. Forgan, C. Froelich, R. Philipona, A. Heimo, G. Koenig-Langlo, B. McArthur, R. Pinker, C.H. Whitlock, K. Dehne, 1998: Baseline Surface Radiation Network (BSRN/WCRP): New precision radiometry for climate research. – Bull. Amer. Meteor. Soc. **79**, 2115–2136, DOI: 10.1175/1520-0477(1998)079<2115:BSRNBW>2.0.CO;2.

Oumbe, A., 2009: Assessment of solar surface radiation using new earth observation capabilities (in French), – Ph.D thesis, MINES ParisTech, 128 pp.

Oumbe, A., Z. Qu, P. Blanc, H. Bru, M. Lefèvre, L. Wald, 2012: Modeling circumsolar irradiance to adjust beam irradiances from radiative transfer models to measurements. – EMS Annual Meeting 2012, 10–14 September 2012, Lodz, Poland.

Oumbe, A., Z. Qu, P. Blanc, M. Lefèvre, L. Wald, S. Cros, 2014: Decoupling the effects of clear atmosphere and clouds to simplify calculations of the broadband solar irradiance at ground level. – Geosci. Model Develop. **7**, 1661–1669, DOI:10.5194/gmd-7-1661-2014, 2014. Corrigendum **7**, 2409–2409.

Percivall, G., L. Ménard, L.-K. Chung, S. Nativi, J. Pearlman, 2011: Geo-processing in cyberinfrastructure: making the web an easy to use geospatial computational platform. – In: Proceedings, 34th International Symposium on Remote Sensing of Environment, 10–15 April 2011, available at: www.isprs.org/proceedings/2011/ISRSE-34/211104015Final00671.pdf, last access: 29 December 2012, Sydney, Australia.

Peuch, V.-H., L. Rouil, L. Tarrason, H. Elbern, 2009: Towards European-scale Air Quality operational services for GMES Atmosphere. – 9th EMS Annual Meeting, EMS2009-511, 9th European Conference on Applications of Meteorology (ECAM) Abstracts, held 28 Sept.–2 Oct. 2009, Toulouse, France.

Qu, Z., 2013: Modeling radiative transfer in cloudy atmosphere to assess surface solar irradiance (in French), – Ph.D thesis, MINES ParisTech, 202 p.

Reinhardt, B., R. Buras, L. Bugliaro, B. Mayer, S. Wilbert, 2012: Circumsolar radiation- a reason for solar resource overestimation – Globally characterized. – EMS Annual Meeting 2012, 10–14 September 2012, Lodz, Poland.

Rigollier, C., M. Lefèvre, L. Wald, 2004. The method Heliosat-2 for deriving shortwave solar radiation from satellite images. – Solar Energy **77**, 159–169.

Roesch, A., M. Wild, A. Ohmura, E.G. Dutton, C.N. Long, T. Zhang, 2011: Assessment of BSRN radiation records for the computation of monthly means. – Atmos. Meas. Tech. **4**, 339–354, DOI:10.5194/amt-4-339-2011, 2011, Corrigendum Atmos. Meas. Tech. **4**, 973–973, DOI: 10.5194/amt-4-973-2011.

Schaaf, C.B., F. Gao, A.H. Strahler, W. Lucht, X.W. Li, T. Tsang, N.C. Strugnell, X.Y. Zhang, Y.F. Jin, J.P. Muller, P. Lewis, M. Barnsley, P. Hobson, M. Disney, G. Roberts, M. Dunderdale, C. Doll, R.P. d'Entremont, B.X. Hu, S.L. Liang, J.L. Privette, D. Roy, 2002: First operational BRDF, albedo nadir reflectance products from MODIS. – Remote Sens. Env. **83**, 135–148, DOI: 10.1016/S0034-4257(02)00091-3.

Schaepman-Strub, G., M.E. Schaepman, T.H. Painter, S. Dangel, J.V. Martonchik, 2006: Reflectance quantities in optical remote sensing: Definitions and case studies. – Remote Sens. Env. **103**, 27–42, DOI:10.1016/j.rse.2006.03.002.

Schade, N.H., A. Macke, H. Sandmann, C. Stick, 2007: Enhanced solar global irradiance during cloudy sky conditions. – Meteorol. Z. **16**, 295–304.

Schulz, J., P. Albert, H.-D. Behr, D. Caprion, H. Deneke, S. Dewitte, B. Dürr, P. Fuchs, A. Gratzki, P. Hechler, R. Hollmann, S. Johnston, K.-G. Karlsson, T. Manninen, R. Müller, M. Reuter, A. Riihelä, R. Roebeling, N. Selbach, A. Tetzlaff, W. Thomas, M. Werscheck, E. Wolters, A. Zelenka, 2009: Operational climate monitoring from space: the EUMETSAT Satellite Application Facility on Climate Monitoring (CM-SAF). – Atmos. Chem. Phys. **9**, 1687–1709, DOI:10.5194/acp-9-1687-2009.

Schutgens, N.A.J., R.A. Roebeling, 2009: Validating the validation: the influence of liquid water distribution in clouds on the intercomparison of satellite and surface observations. – J. Atmos. Ocean. Technol. **26**, 1457–74, DOI: 10.1175/2009jtecha1226.1.

Shiobara, M., S. Asano, 1993: Estimation of cirrus optical thickness from sun photometer measurements. – J. Appl. Meteor. **33**, 672–681, DOI:10.1175/1520-0450(1994)033<0672:EOCOTF>2.0.CO;2.

Tarpley, J., 1979: Estimating incident solar radiation at the surface from geostationary satellite data. – J. Appl. Meteor. **18**, 1172–1181.

Trewartha, G.T., 1954: An Introduction to Climate, 3rd Edn. – McGraw Hill Book Co.

Vermote, E.F., D. Tanré, J.L. Deuzé, M. Herman, J.-J. Morcrette, 1997: Second simulation of the satellite signal in the solar spectrum: An overview, IEEE T. – Geosci. Remote Sens. **35**, 675–686.

WDC, 2015: Cloud physical parameters from SEVIRI at WDC-RSAT. – http://wdc.dlr.de/data_products/CLOUDS/clouds_seviri.php.

WMO, 2008: Guide to meteorological instruments and methods of observation. – World Meteorological Organization, WMO-No **8**, 7th Ed. Geneva, Switzerland.